LIGHT NUCLEI PRODUCTION IN A DYNAMICAL MODEL FOR A QCD PHASE TRANSITION

THIRANAT BUMNEDPAN

A Thesis Submitted in Partial Fulfillment of the Requirements for the

Degree of Master of Science in Physics

Suranaree University of Technology

Academic Year 2024

ผลผลิตของนิวเคลียสเบาในแบบจำลองพลวัตสำหรับการเปลี่ยนแปลงวัฏภาคของกระบวนการควอนตัมโครโมไดนามิกส์

นายถิรณัฐ บำเหน็จพันธุ์

วิทยานิพนธ์นี้เป็นส่วนหนึ่งของการศึกษาตามหลักสูตรปริญญาวิทยาศาสตรมหาบัณฑิต

สาขาวิชาฟิสิกส์

มหาวิทยาลัยเทคโนโลยีสุรนารี

ปีการศึกษา 2567

LIGHT NUCLEI PRODUCTION IN A DYNAMICAL MODEL FOR A QCD PHASE TRANSITION

Suranaree University of Technology has approved this thesis submitted in partial fulfillment of the requirements for a Master's degree.

Thesis Examining Committee

(Prof. Dr. Yupeng Yan)
Chairperson

(Assoc. Prof. Dr. Christoph Herold)
Member (Thesis Advisor)

(Dr. Jan Steinheimer)
Member (Thesis Co-advisor)

(Assoc. Prof. Dr. Ayut Limphirat)
Member

(Assoc. Prof. Dr. Tirawut Worrakitpoonpon)
Member

(Assoc. Prof. Dr. Yupaporn Ruksakulpiwat)
Vice rector for Academic Affairs
and Quality Assurance

(Prof. Dr. Santi Maensiri)
Dean of Institute of Science

ถิรณัฐ บำเหน็จพันธุ์ : ผลผลิตนิวเคลียสเบาในแบบจำลองพลวัตสำหรับการเปลี่ยนแปลงวัฏภาคของกระบวนการควอนตัมโครโมไดนามิกส์ (LIGHT NUCLEI PRODUCTION IN A DYNAMICAL MODEL FOR A QCD PHASE TRANSITION)
อาจารย์ที่ปรึกษา : รองศาสตราจารย์ ดร.คริสทอฟ แฮโรลด์, 57 หน้า.

คำสำคัญ : การชนของไอออนหนัก/ การเปลี่ยนแปลงวัฏภาค/ แบบจำลองการชนของไอออนหนัก UrQMD/ นิวเคลียสเบา/ ความผันผวน/ คิวมูแลนต์

แบบจำลองการชนของไอออนหนัก UrQMD ที่ใช้สมการสภาวะซึ่งขึ้นกับความหนาแน่นรวมไปถึงการเปลี่ยนแปลงสถานะลำดับที่หนึ่งถูกนำมาใช้ศึกษาการวิวัฒน์ของความอ่อนไหวของจำนวนแบรีออนและจำนวนโปรตอนจนถึงลำดับที่สาม ในปฏิกิริยาการชนของไอออนหนักที่พลังงาน $E_{\text{lab}} = 2.0 - 3.0\ A\text{GeV}$ เราพบความเบี่ยงเบนจากการกระจายตัวแบบเกาส์เซียนอย่างมีนัยสำคัญที่สามารถเห็นได้ชัดของความแปรปรวนของจำนวนแบรีออนในปริภูมิเชิงพิกัด ในทางกลับกันนั้น ความแปรปรวนของจำนวนโปรตอนมักถูกกดทับไว้ เนื่องจากจำนวนของโปรตอนนั้นมีสัดส่วนเพียงเล็กน้อยเมื่อเทียบกับจำนวนแบรีออนทั้งหมดในช่วงที่ระบบอยู่ในสภาวะที่หนาแน่นซึ่งเป็นสถานะเริ่มต้นของการชน เราพบว่าสัญญาณเพียงเล็กน้อยอย่างเดียวที่สามารถวัดได้ คือการเพิ่มขึ้นของคูมูแลนต์ลำดับที่สามหรือสูงกว่า ของจำนวนโปรตอนในช่วงของแรพิดิตี (Δy) ที่มีขนาดมากกว่าหนึ่งหน่วย นอกจากนี้ยังพบว่าความแปรปรวนของจำนวนอนุภาคในปริภูมิเชิงพิกัดจะนำไปสู่การเพิ่มจำนวนการเกิดคลัสเตอร์เนื่องจากค่าสหสัมพันธ์ในปริภูมิเชิงพิกัดที่เพิ่มขึ้น อย่างไรก็ตาม การเพิ่มขึ้นนี้มีค่าน้อยมาก และส่วนใหญ่จะเกิดในช่วงที่ระบบยังมีความหนาแน่นสูง ซึ่งเป็นช่วงเวลาก่อนที่ระบบจะเข้าสู่สภาวะที่ไม่มีการชนของอนุภาคแล้ว

สาขาวิชาฟิสิกส์
ปีการศึกษา 2567

ลายมือชื่อนักศึกษา ถิรณัฐ บำเหน็จพันธุ์
ลายมือชื่ออาจารย์ที่ปรึกษา
ลายมือชื่ออาจารย์ที่ปรึกษาร่วม

THIRANAT BUMNEDPAN : LIGHT NUCLEI PRODUCTION IN A DYNAMICAL MODEL FOR A QCD PHASE TRANSITION. THESIS ADVISOR : ASSOCIATE PROFESSOR CHRISTOPH HEROLD, Ph.D. 57 PP.

Keywords: Heavy-ion collision/ phase transition/ UrQMD model simulation/ light nuclei/ fluctuation/ cumulants

The UrQMD model, incorporating a density-dependent equation of state with a first-order phase transition, is employed to investigate the time evolution of baryon and proton number susceptibilities up to third order in heavy-ion collisions at $E_{\text{lab}} = 2.0 - 3.0$ AGeV. Notably, baryon number fluctuations in coordinate space show significant deviations from Gaussian behavior. In contrast, proton number fluctuations are consistently suppressed, as protons represent only a small portion of the total baryon number during the high-density phase of the reaction. The analysis indicates that the only potentially observable—though weak—signal is an enhancement of third-order (or higher) proton cumulants within a finite rapidity window $\Delta y > 1$. Additionally, spatial fluctuations are found to promote cluster formation due to enhanced correlations in coordinate space, but this effect remains modest and primarily occurs in the early dense stage of the collision before freeze-out.

School of Physics
Academic year 2024

Student's signature ถิรนัฏ บำเหน็จพันธุ์
Advisor's signature
Co-advisor's signature

ACKNOWLEDGEMENTS

First of all, I would like to express my gratitude to Assoc. Prof. Dr. Christoph Herold (very first daddy) for his supervision and many possible opportunities he has given to me. I appreciate your welcoming attitude and your willingness to answer my numerous questions, constructing me from the scratch.

I deeply admire and respect Dr. Jan Steinheimer (another master daddy) for his substantial contributions and the inspiration behind this research, as we have collaborated on this project. Outstanding ideas and solutions consistently emerged from him. Furthermore, he took good care of me while I was going through the visa approval process until my arrival in Germany, which made me truly cherish the research experience during that time.

This research is supported by the Development Promotion of Science and Technology (DPST) scholarship and the Center of Excellence in High Energy Physics & Astrophysics, Suranaree University of Technology.

Thiranat Bumnedpan

CONTENTS

CONTENTS (Continued)

LIST OF FIGURES

LIST OF FIGURES (Continued)

Figure **Page**

LIST OF FIGURES (Continued)

Figure **Page**

LIST OF FIGURES (Continued)

Figure **Page**

CHAPTER I

INTRODUCTION

The primary focus in heavy-ion collision experiments is the detection of a possible QCD phase transition in dense baryonic matter. Specifically, the transition between a phase, known also as the QGP, which is also characterized by chiral symmetry restoration, and the confined phase of nuclear matter where chiral symmetry is spontaneously broken. We aim to study this transition in the context of a rapidly expanding fireball of hot and dense nuclear matter created during heavy-ion collision experiments. In such a scenario the rapid phase separation will lead to enhanced fluctuations and clustering of the baryon number, related to an increment of the baryon number susceptibilities.

In recent studies of heavy-ion collisions have highlighted the utility of light nuclei cumulants as sensitive observables for probing the QCD phase structure, particularly in the search for a critical point and phase transition signals. Theoretical investigations employing transport models, such as the Ultra-relativistic Quantum Molecular Dynamics (UrQMD) (Bleicher et al., 1999) framework with a density-dependent equation of state incorporating a first-order phase transition, have demonstrated substantial deviations from Gaussian fluctuation patterns in the cumulants of baryon number and light nuclei yields. These deviations are attributed to enhanced coordinate-space correlations and clustering effects in the vicinity of a phase boundary (Bumnedpan, Steinheimer, Reichert, et al., 2025) Complementary experimental measurements from the STAR collaboration at RHIC, particularly within the Beam Energy Scan program, have reported non-monotonic behavior in higher-order proton cumulants as a function of collision energy, consistent with theoretical expectations of critical phenomena. Collectively, these findings underscore the potential of light nuclei cumulants as robust signatures of critical behavior and phase transitions in strongly interacting matter.

The present work uses the Ultra-relativistic Quantum Molecular Dynamics (UrQMD) transport model together with the coalescence model to study potential enhancements of light nuclear cluster production, due to enhanced fluctuations, at a QCD first-order phase transition. The formation of clusters in UrQMD is based on the coalescence model, a phenomenological model of light nuclei formation based on the Wigner wave function formalism, where sufficiently close momenta and positions of protons and neutrons, after the chemical freeze-out, lead to light nuclei formation. Besides protons (p), the light nuclei of interest include deuteron (d), triton (t), helium-3 (^3He), and helium-4 (^4He). We will calculate their yields both within a spatial central volume and in momentum space by applying typical experimental cuts in rapidity and transverse momentum. We study the time evolution of the respective multiplicity for various energies and their maximum enhancement as a function of beam energy to search for potential enhancements as a consequence of a phase transition at low- to intermediate energies. Additionally, we will investigate the proton number variance and skewness which is also sensitive to a phase transition.

CHAPTER II

LITERATURE REVIEW

The upcoming sections will provide insight into the quark-gluon plasma and the QCD phase diagram created by heavy-ion collision experiments. Additionally, it will cover the models utilized for the light nuclei production.

2.1 Heavy-ion collision

The main goals of heavy-ion collision experiments are to understand the nonperturbative aspects of QCD and create and probe a new state of matter called quark-gluon-plasma (QGP) which can be observed in collisions at sufficiently large center-of-mass energies (STAR Collaboration: J. Adams, 2005). In heavy-ion collisions, nuclei are accelerated to nearly the speed of light before they collide with each other. The time evolution of such a ultra high-energy collision usually is divided into four states as follows. First, thermalization occurs shortly after ($\sim$ 1 fm) the collision when a locally thermalized QGP is created, with quarks and gluons as relevant degrees of freedom. Second, during hadronization, hadrons begin to form out of the QGP medium. As time passes and the temperature decreases, the system reaches a state of chemical freeze-out. In this state, inelastic particle collisions cease, and no new particles are created, resulting in fixed particle multiplicities. The time evolution progresses to the final stage known as kinetic freeze-out, where elastic particle collisions come to an end, causing fixed particle spectra as they are measured by detectors (see figure 2.1).

In the beam energy regime where one expects to encounter a phase transition in QCD during the evolution such a schematic picture is not valid anymore. Most importantly, the initial compression phase, which is most sensitive on the underlying equation of state, cannot be treated independently from the bulk evolution. In addition the equilibrium phase and subsequent hadronic stage are highly intertwined. To be able to describe a phase transition in such a complex many body system the use of state-of-the-art microscopic transport simulations is necessary.

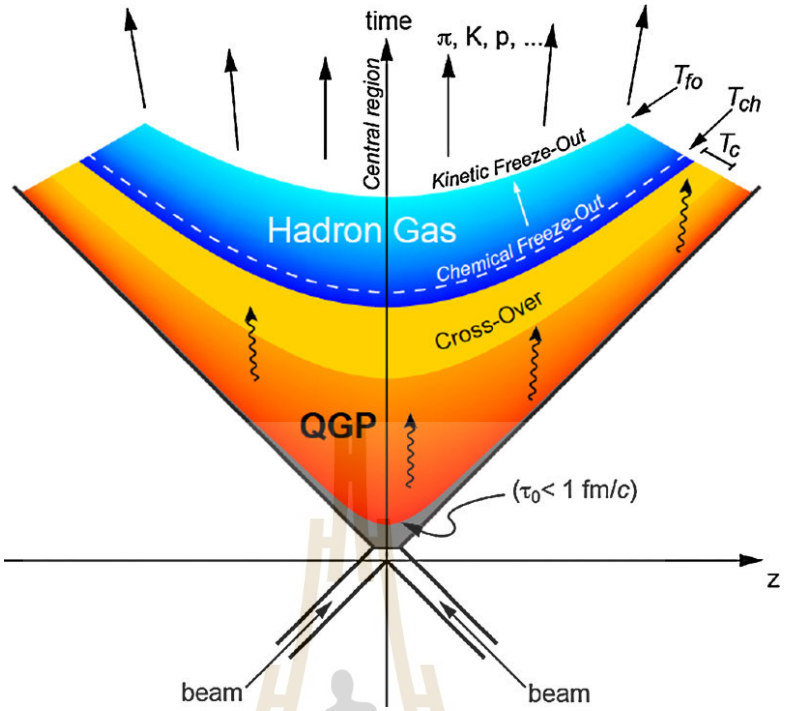

Figure 2.1 The space-time diagram of heavy-ion collision (Braun-Munzinger et al., 2019).

2.2 Quantum chromodynamics phase transition

The existence of a medium of deconfined quarks and gluons is expected at high temperature and/or density. As a consequence, this gives rise to an investigation of possible phase transition between confinement and deconfinement state as seen in the phase diagram of QCD (see figure 2.2).

As previously stated, during the hadronization process, the QGP matter undergoes the transition process, deconfined quarks are formed into hadronic matter. In heavy-ion collision experiments, the process of identifying a phase transition can be performed by several measurements through a variety of observables. These measurements, including fluctuations in particle counts (hadron multiplicities), their transverse momentum, and the mean transverse energy, serve as key indicators (Sasaki et al., 2007). Through an analysis of these fluctuations, one can effectively derive critical parameters such as the critical temperature and baryochemical potential from the equation of state as depicted within the Quantum Chromodynamics (QCD) phase diagram. Notably, as the critical point where the first-order phase transition terminates, these fluctuations are expected to be greatly enhanced. Experimentally, STAR (Abdallah et al., 2025), NA49/61 (Grebieszkow, 2009; Andronov, 2019), and for lowest energies, also the HADES

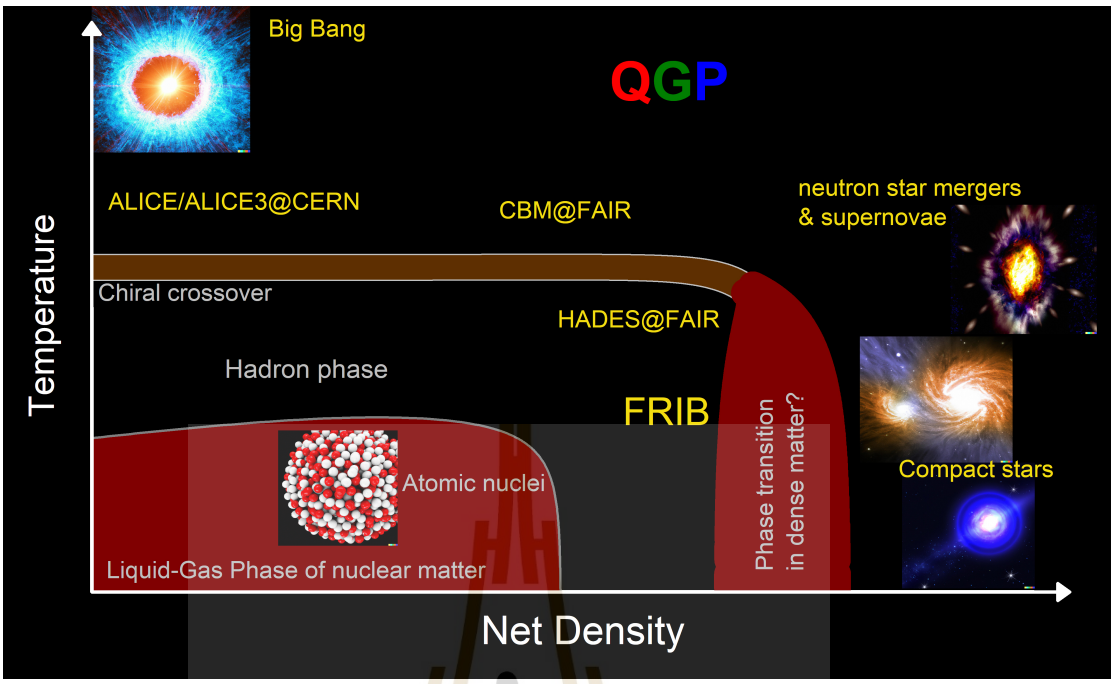

Figure 2.2 The phase diagram of quarks and gluons. The diagram displays the current knowledge and assumptions on possible states that quarks and gluons can become as function of temperature *T* and baryon density (image by Jan Steinheimer).

collaboration (Adamczewski-Musch et al., 2020) have provided data which so far have not been able to allow us a final conclusion about the existence of a QCD critical point and first-order phase transition.

Investigation of the phase transition in collision experiments can also be conducted through simulation models including chiral fluid dynamics. This is a model that accounts the QGP matter as a fluid undergoing a hydrodynamic expansion. The time evolution in the chiral order parameter implies a transition between chiral symmetry breaking and restoration. Entropy production (Herold, Kittiratpattana, et al., 2019) and enhancement in hadron multiplicity ratios have been identified as potential probes of a phase transition (Bumnedpan, Steinheimer, Bleicher, et al., 2022).

The order of the QCD transition for vanishing baryochemical potential has been unambiguously identified as a crossover rather than a phase transition using lattice QCD (Aoki et al., 2006). In this discretization of QCD on a lattice of finite volume, the QCD partition function can be computed directly, leading to the thermodynamic quantities sensitive to a phase transition like the chiral condensate as the potential order parameter or the chiral susceptibility.

As a consequence, a divergence of the susceptibility, in infinite matter, indicates the location of a phase transition (Karsch, 2017; Bazavov et al., 2020).

For finite chemical potential, lattice QCD suffers from the sign problem which makes direct calculations impossible. Alternative approaches include functional techniques using Dyson-Schwinger equations for the couple quark and gluon propagators (Fischer et al., 2014; Gao et al., 2021) or low-energy effective models, often base on the linear sigma or Nambu-Jona-Lasinio (NJL) models which both describe spontaneous chiral symmetry breaking by the QCD ground state (Scavenius et al., 2001; Schaefer et al., 2005; Fukushima, 2008). The location of the CEP has been estimated from functional techniques and also effective models, so far, however, with only little agreement between the various theoretical approaches.

2.3 Equation of state: EoS

An equation of state (EoS) is the relationship that links the various thermodynamics quantities, providing insight into how a macroscopic system behaves under different conditions. It is an essential input for any hydrodynamic model and contains information on the phase transition. For the purpose of heavy-ion collisions, we are going to introduce the grand canonical partition function

$$Z(T,V,\mu) = \sum_{N=0}^{\infty} \frac{1}{h^{3N}} \int d^{3N}x \int d^{3N}p \, \mathrm{e}^{\frac{-(H(x_\nu,p_\nu)-\mu N)}{T}} \,, \tag{1}$$

and the grand potential density

$$\Phi(T,V,\mu) = -\frac{T}{V} \ln Z = -P \,, \tag{2}$$

with the thermodynamics relation

$$\Phi(T,V,\mu) = \varepsilon - Ts - \mu n \,. \tag{3}$$

Here, ε, s, μ, and n represent energy density, entropy density, chemical potential, and particle number density, respectively.

In hyperspace, denoted by x_ν and p_ν, the positions and momenta are represented as $x_\nu = x_1, x_2, x_3, ..., x_N$ and $p_\nu = p_1, p_2, p_3, ..., p_N$, respectively. Here, H refers to the Hamiltonian. After determining the grand partition function, the mean particle number is can be calculated using the expression

$$\begin{aligned}\langle N\rangle &= \frac{1}{Z}\sum_{i=0}^{\infty} N\mathrm{e}^{\frac{-(E_i-\mu N)}{T}} = \left.\frac{\partial(T\ln Z)}{\partial\mu}\right|_{T,V} = -\left.\frac{\partial\Phi}{\partial\mu}\right|_{T,V} \\ &= \left.\frac{T}{Z}\frac{\partial Z}{\partial\mu}\right|_{T,V}. \end{aligned} \tag{4}$$

From now on, we will express all the quantities in natural units i.e., the Boltzmann constant $k = 1$.

For indistinguishable particles, the grand partition function becomes

$$\begin{aligned} Z(T,V,\mu) &= \sum_{i=0}^{\infty}\frac{1}{N!h^{3N}}\int d^{3N}x\int d^{3N}p\ \mathrm{e}^{-\frac{H-\mu N}{T}} \\ &= \sum_{i=0}^{\infty}(\mathrm{e}^{\mu/T})^N Z_c(T,V,N). \end{aligned} \tag{5}$$

Where $Z_c(T,V,N)$ is the canonical partition function. It can be seen that the grand partition function is weighted over the summation by a factor of $e^{\mu/T}$, this factor is later defined as the fugacity in which $e^{\mu/T} \equiv \lambda$.

In the context of non-interacting particles in a system, the expression of the canonical partition function can be rewritten in term of a partition function for one particle,

$$Z_c(T,V,N) = \frac{1}{N!}[Z_c(T,V,1)]^N. \tag{6}$$

The grand canocical partition function for non-interacting particles then becomes

$$Z(T,V,\mu) = \sum_{N=0}^{\infty} \frac{1}{N!}(\mathrm{e}^{\mu/T})^N [Z_c(T,V,1)]^N$$
$$= \sum_{N=0}^{\infty} \frac{1}{N!}(\lambda)^N [Z_c(T,V,1)]^N$$
$$Z(T,V,\mu) = \mathrm{e}^{\lambda Z_c(T,V,1)}. \quad (7)$$

This form of the partition function can then be applied in a situation of relativistic ideal gas of identical particle. The Hamiltonian describing a relativistic ideal gas is expressed as

$$H = \sum_{i=0}^{N} E_i = \sum_{i=0}^{N} \sqrt{p_i^2 + m_i^2} \quad (8)$$

Then the canonical function for one particle becomes

$$Z_c(T,V,1) = \frac{1}{h^3} \int d^3x \int d^3p \, \mathrm{e}^{-\frac{\sqrt{p^2+m^2}}{T}}$$
$$= \frac{V}{2\pi^2} \int_0^{\infty} p^2 dp \, \mathrm{e}^{-\frac{\sqrt{p^2+m^2}}{T}}$$
$$Z_c(T,V,1) = \frac{V}{4\pi^2} \int_0^{\infty} \frac{m^3}{2} \sinh(t)\sinh(2t) e^{-\frac{m}{T}\cosh(t)} dt \quad (9)$$

The integral could be carried out by interchanging the variables: $\frac{p}{m} = \sinh(t)$ and $dp = m\cosh(t)$.

After determining the canonical partition function for a single particle, we can progress to calculate the grand partition function, Z, by applying the thermodynamic relationship as outlined in equation (3).

2.4 Correlations and fluctuations

The baryon number fluctuations arising from phase separation during a non-equilibrium first-order phase transition can be analyzed using the cumulants of multiplicity distributions within a fixed spatial volume. In this study, we focus on the cumulants C, which are closely related to the factorial cumulants employed in previous works (Skokov et al., 2013; Bzdak and Koch, 2019) and encapsulate essentially the same information. The first three cumulants are defined as follows:

$$C_1 = \langle N \rangle = \mu \tag{10}$$

$$C_2 = \sigma^2 = N^2 - \langle N \rangle^2 \tag{11}$$

$$C_3 = S\sigma^3 = \langle (N - \langle N \rangle)^3 \rangle \tag{12}$$

where μ is event averaged particle mean expectation value, S is the skewness and σ^2 is variance, the $\langle \cdot \rangle$ symbol denotes event-average quantity. In this work, we shall calculate the time dependence of proton number cumulants up to the 3rd order for beam energies 2.0 AGeV and 3.0 AGeV.

Given that cumulants scale linearly with system volume to first order, it is common practice to use their ratios to cancel out this volume dependence:

$$\frac{C_2}{C_1} = \frac{\sigma^2}{\mu} \tag{13}$$

$$\frac{C_3}{C_2} = S\sigma \tag{14}$$

The observed ratios are influenced by various features of the collision dynamics, not only by the presence of a phase transition. Three key factors that play a crucial role are fluctuations in the number of participants (Skokov et al., 2013), accurate handling of experimental acceptance, and corrections for experimental efficiency (Luo et al., 2019). In this study, we largely neglect these effects, as accurately accounting for them would demand detailed information about a specific detector setup, centrality determination procedure, and associated corrections. Instead, we focus on signals that remain visible even when volume fluctuations are included, assuming these are more likely to be experimentally observable. In contrast, signals that emerge only after substantial (and

sometimes model-dependent) corrections may not be entirely reliable.

2.5 Experimental results

As far as we have been mentioning the enhancements of the cluster as a signal for the phase transition from our simulation model, we now aim to show the cluster fluctuations via cumulant ratio observed at the relativistic heavy ion collider (RHIC) in the STAR collaboration experiment (see figure 2.3). Figure 2.3 shows the cumulant ratio C_4/C_2 for various collision systems, compared with results from UrQMD simulations. The data are consistent with the model employing an equation of state without a phase transition, further results are to be anticipated in the future compressed baryonic experiment at FAIR.

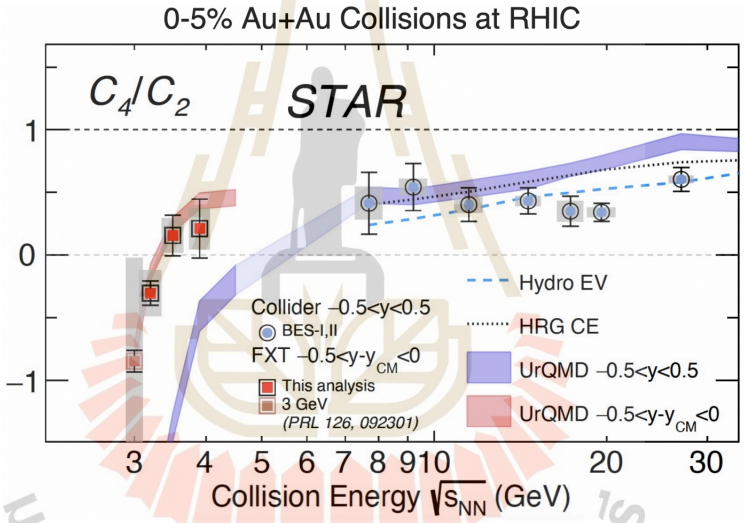

Figure 2.3 The proton cumulant ratio C_4/C_2 in two beam energy scan phases BES-I and BES-II at RHIC in different centralities under AuAu collision within rapidity range $|y| < 0.5$ (image taken from the Quark Matter 2025 in Frankfurt by Zachary Sweger, Wed, P35).

Another set of experimental results on the beam-energy-dependent cumulant ratios that we would like to represent comes from the STAR together with the HADES collaboration as displayed in figure 2.4. We hereby emphasize the result regarding the ratio K_3/K_2 (which is equivalent to $C_3/C_2 = S\sigma$ in this work). The data from STAR in the 0–5% centrality class (red circles), along with the 0–10% HADES data (red square), illustrate the trend of cumulant ratios across a wide range of collision energies—from the lowest accessible energies to the high-energy regime. Nevertheless, the data is still being collected and will be subject to further corrections in the upcoming CBM experiment.

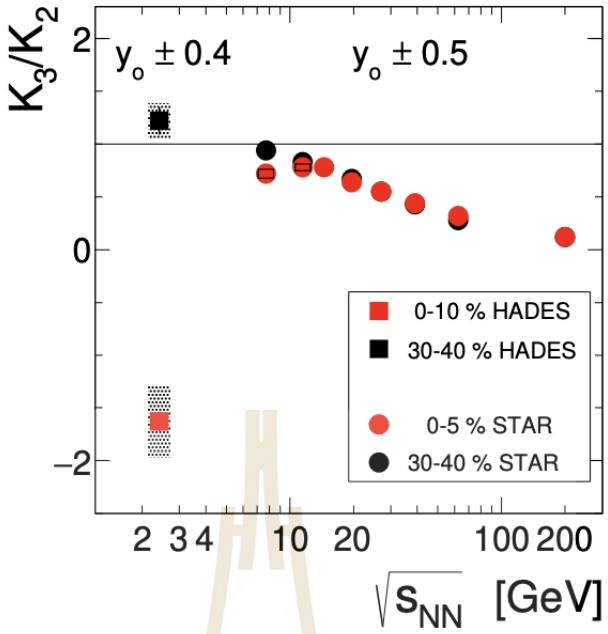

Figure 2.4 Beam energy dependence of the scaled cumulant K_3/K_2 in different centralities including a comparison with the STAR data (Adamczewski-Musch et al., 2020)

2.6 Light nuclei production

The production of the light nuclei: protons, deuterons, ^3He, and ^4He is employed as a probe for the first-order phase transitions. An enhanced light nuclei production as well as their double ratios implies a signal of the phase transition due to the emergence of local density fluctuations as the medium undergoes a dynamical first-order phase transition (Steinheimer and Randrup, 2012; Herold, Nahrgang, et al., 2014; Steinheimer, Randrup and Koch, 2014; Sun, Chen, Ko, Pu, et al., 2018; Sun, Ko, et al., 2021). With a focus on the result from (Sun, Ko, et al., 2021) in figure 2.5, the enhancement in the double ratio $(N_t * N_p)/d^2$ as a function of coupling strength g_V in the Lagrangian describing flavor-independent interaction of quarks. A peak structure can be clearly seen, indicating the first-order phase transition.

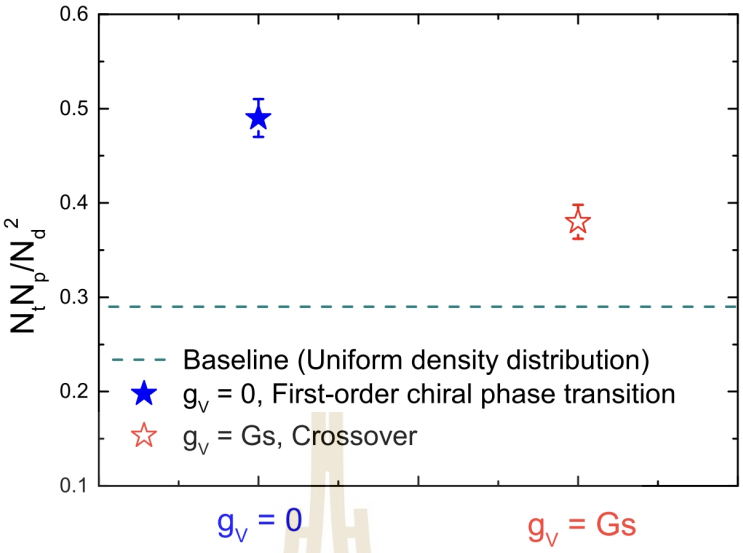

Figure 2.5 Double ratio of triton (t), proton (p) and deuteron (d) as a function of coupling strength with the case of first-order phase transition (blue solid star) and crossover (red open star) (Sun, Ko, et al., 2021)

The following sections will provide a further explanation of the model regarding the production of the light nuclei.

2.6.1 Coalescence model

The formation of nuclei can be described by the coalescence model (Sun, Chen, Ko and Xu, 2017), a phenomenological model of light nuclei formation after the kinetic freeze-out. The concept of light nuclei formation involves the merging of protons and neutrons with nearly identical momentum and positions, defined by cutoff values for relative momenta and positions.

Our research focuses on understanding of the QCD first-order phase transition as it is expected to occur in the QCD phase diagram for large values of the baryochemical potential and, consequently, low to intermediate energies in heavy-ion collision experiments. As a potential signal for a first-order transition, we are mainly interested in the light nuclei production.

The momentum-space coalescence is a way to describe how particles with specific momenta come together to form larger particles or clusters based on their momentum characteristics. The expression of momentum-space coalescence is given

by (Dover et al., 1991)

$$N_c = g_c \int \left(\prod_{i=1}^{N} dN_i \right) f_c^W(\overrightarrow{r}_1, \cdots, \overrightarrow{r}_N, \overrightarrow{p}_1, \cdots, \overrightarrow{p}_N) \ , \tag{15}$$

where $f_c^W(\overrightarrow{r}_1, \cdots, \overrightarrow{r}_N, \overrightarrow{p}_1, \cdots, \overrightarrow{p}_N)$ is the Wigner function which is proportional to the coalescence probability, and g_c is the coalescence factor.

2.6.2 Thermal model

The thermal model, also known as the statistical model, is a model used to calculate the particle production yield (multiplicity) at the chemical freeze-out by assuming an equilibrated global heat bath out of which all particles are produced at a common temperature T, volume V, and baryochemical potential μ_B. The logarithm of the grand canonical partition function of particle species i is expressed in the form

$$\ln Z_i = \begin{cases} \dfrac{V g_i}{2\pi^2} \displaystyle\int_0^\infty p^2 dp \ln\left(1 + \lambda_i \mathrm{e}^{-E_i/T}\right) & \text{for fermions ,} \\ \dfrac{-V g_i}{2\pi^2} \displaystyle\int_0^\infty p^2 dp \ln\left(1 - \lambda_i \mathrm{e}^{-E_i/T}\right) & \text{for bosons ,} \end{cases} \tag{16}$$

with $\mu_i = B_i\mu_B + S_i\mu_s + Q_i\mu_Q$, the chemical potential of particle species i being expressed as a linear combination of the chemical potential of a certain quantity as follows: B for baryon number, S for strangeness and Q for electric charge. Here, $\lambda_i = e^{\mu_i/T}$ is the fugacity of particle species i, g_i is the degeneracy, and E_i denotes the relativistic energy. With a known partition function, the pressure and the particle number density can be calculated,

$$P_i = \frac{T}{V}\ln Z_i = \begin{cases} \dfrac{Tg_i}{2\pi^2}\displaystyle\int_0^\infty p^2 dp \ln\left(1+\lambda_i \mathrm{e}^{-E_i/T}\right) & \text{for fermions ,} \\ \dfrac{-Tg_i}{2\pi^2}\displaystyle\int_0^\infty p^2 dp \ln\left(1-\lambda_i \mathrm{e}^{-E_i/T}\right) & \text{for bosons ,} \end{cases} \tag{17}$$

$$n_i = \frac{\partial P_i}{\partial \mu_i} = \begin{cases} \dfrac{g_i}{2\pi^2}\displaystyle\int_0^\infty \frac{p^2 dp}{1+\mathrm{e}^{(E_i-\mu_i)/T}} & \text{for fermions ,} \\ \dfrac{g_i}{2\pi^2}\displaystyle\int_0^\infty \frac{p^2 dp}{1-\mathrm{e}^{(E_i-\mu_i)/T}} & \text{for bosons .} \end{cases} \tag{18}$$

To eliminate the dependence on the source volume V as an additional fit parameter to the thermal model, particle number ratios are often used rather than absolute numbers,

$$\frac{N_i}{N_j} = \frac{n_i V}{n_j V} = \frac{n_i}{n_j}. \tag{19}$$

With this relationship, experimental measurements of particle number ratios can be compared with the model's predictions. The thermal model has successfully reproduced hadron and light nuclei yields over a wide range of beam energies and experiments (Albright et al., 2015; Biswas, 2020; Bhattacharyya et al., 2021).

2.7 Fluctuations in coordinate vs. momentum space

Density fluctuations in coordinate space arise from local variations in energy, pressure, or temperature during heavy-ion collisions. These fluctuations may result from phase transitions or inhomogeneities in the initial conditions. Effects such as collective flow and particle rescattering can dilute or distort the original fluctuation patterns. Nevertheless, the signals can become more pronounced under certain conditions, particularly when fluctuations occur near the freeze-out stage or when the medium exhibits low viscosity. Observables such as higher-order cumulants (e.g., $S\sigma$ and $K\sigma^2$) and particle yield ratios involving light nuclei are especially sensitive to these effects.

The result of a relation between the corrected scaled variance of the particle number within the rapidity acceptance and the fixed acceptance fraction (Kuznietsov et al., 2024) has shown that the limiting cases for the result in coordinate space can only be consistent with high collision energy $\sqrt{s_{NN}} = 5,020$ GeV (see figure 2.6).

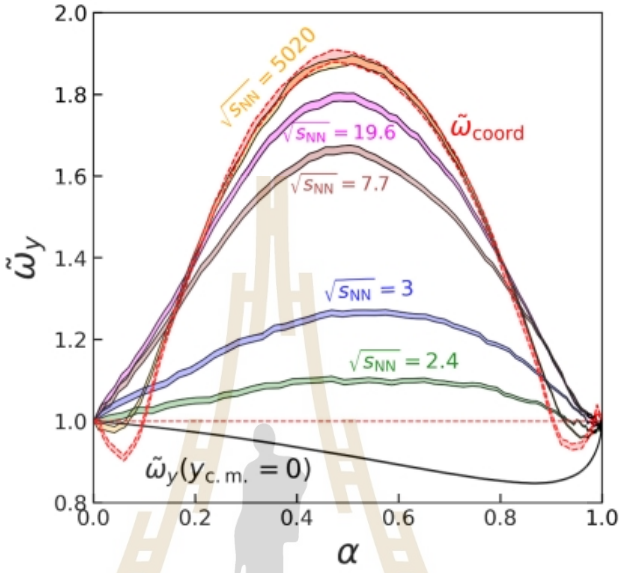

Figure 2.6 Corrected scaled variance $\tilde{\omega}_y$ as a function of fixed acceptance fraction α_y. The bands correspond to the beam energies $\sqrt{s_{NN}}$. The limiting cases of coordinate space are shown in red band, labeled $\tilde{\omega}_{coord}$ (Kuznietsov et al., 2024).

CHAPTER III

RESEARCH METHODOLOGY

This section outlines the research methodology, including simulations using the UrQMD program and the implementation of light nuclei formation within the framework, followed by details on data analysis. In addition, the UrQMD simulation model is introduced.

3.1 The UrQMD transport model

The Ultrarelativistic Quantum Molecular Dynamics model (UrQMD) is a microscopic simulation model employed for (ultra)relativistic heavy-ion collisions across an energy spectrum spanning from Bevalac and SIS up to AGS, SPS, and RHIC. Its primary objectives encompass achieving a deeper comprehension of various aspects, including the formation and characteristics of dense hadronic matter at elevated temperatures, properties of nuclear matter and resonance states, the generation of mesonic matter and antimatter, as well as the production and transport of rare particles within hadronic matter. Additionally, UrQMD is instrumental in studying the creation, modification, and annihilation of strangeness in matter, along with the emission of electromagnetic probes (Bass et al., 1998; Bleicher et al., 1999). For our simulation of heavy-ion collisions, we utilize the UrQMD model, which incorporates a coalescence model for the dynamic formation of nuclei from protons and neutrons with identical momenta and positions. In our simulation, the program was in version 3.4 and we also configured the model to operate in coalescence mode, considering projectile masses corresponding to a mass of 197 (the mass of Au, gold). We conducted a simulation of Au+Au collisions from t =1 fm/c until 60 fm/c across a range of beam energies from 2.0 AGeV to 3.0 AGeV with 1.0 AGeV increment.

This model incorporates a density-dependent Equation of State (EoS) by introducing an effective density-dependent potential into the non-relativistic Quantum Molecular Dynamics (QMD) (Aichelin et al., 1986; Hartnack et al., 1989; Stoecker et al., 1986) equations of motions,

$$\dot{\mathbf{r}}_i = \frac{\partial H}{\partial p_i}, \qquad \dot{p}_i = -\frac{\partial H}{\partial r_i}. \tag{20}$$

In this context, the total Hamiltonian of the system, denoted as H, encompasses both the kinetic energy and the overall potential energy, which can be expressed as $V = \sum_i V_i \equiv \sum_i V\big(n_B(r_i)\big)$. The equations of motion are then solved, taking into account that the potential energy V is straightforwardly related to the pressure (Steinheimer, Motornenko, et al., 2022).

$$P(n_B) = P_{\text{id}}(n_B) + \int_0^{n_B} n' \frac{\partial U(n')}{\partial n'} dn' \tag{21}$$

Here, $P_{\text{id}}(n_B)$ represents the pressure of an ideal Fermi gas of baryons, and $U(n_B) = \frac{\partial\big(n_B \cdot V(n_B)\big)}{\partial n_B}$ denotes the single particle potential.

3.2 Implementation of a phase transition in UrQMD

Implementing a phase transition into the CMF model, involves a straightforward modification (Savchuk et al., 2023). To introduce an additional meta-stable state within the mean field energy per baryon at high densities, apart from the existing bound state resulting from the nuclear liquid-gas transition, an adjustment is made to the original chiral mean field (CMF) potential. This adjustment consists of truncating the potential at a density of $2.6\, n_0$. Beyond this density threshold, the potential $V(n_B)$ is then shifted by an amount $\Delta n_B = 2.6\, n_0$.

The selection of the n_{cut} value is influenced by two key considerations:

1. To ensure the attainability of the transition through heavy ion collision experiments, it is essential to restrict the density range to $n_B^{cut} < 4 - 5 n_0$ (Omana Kuttan et al., 2022).
2. The chosen density surpasses the threshold of $2 n_0$ to prevent any inconsistencies with the existing constraints derived from heavy ion collisions and observations in astrophysical contexts (Huth et al., 2022).

The mean field energy within the range of $n_B^{cut} < n_B < n_B^{cut} + \Delta n_B$ is interpolated using a third-order polynomial. This interpolation is carried out to establish a secondary minimum in the energy per particle, denoted as $V(n_B)$. This approach guarantees the continuity of both the energy function and its derivative.

Figure 3.1 represents the evolution in the pressure and net baryon density at $T = 0$ compared to the normal CMF EoS and the implemented phase transition EoS. The red shading area corresponds to the region of mechanical instabilities, where the system created after a collision rapidly separated into the two coexisting phases. This

mechanism is known as spinodal decomposition. One can observe a non-monotonic behavior in the blue line, which reflects the nature of the phase transition.

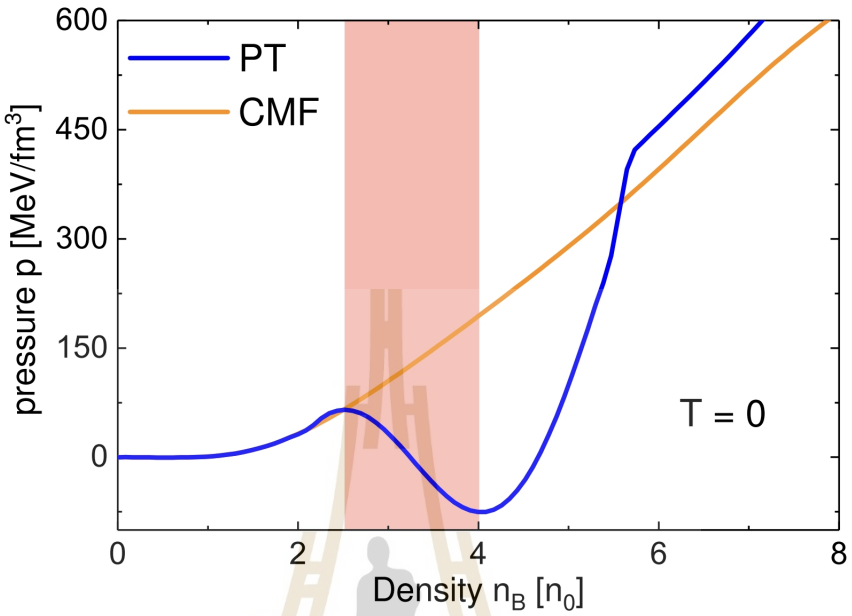

Figure 3.1 Time evolution in pressure and baryon density at $T = 0$ between the two scenarios: the CMF EoS with no phase transition (orange line) and the phase transition EoS (blue line). The red shading area refers to a region where the pressure gradient is negative: the spinodal region (Savchuk et al., 2023).

3.3 Light nuclei production in UrQMD

3.3.1 Deuteron production

The implementation of phase-space coalescence done in UrQMD for deuterons in the following way (Sombun et al., 2019):

1. Throughout the system's time evolution, we track the trajectories of protons and neutrons until the specific spacetime coordinates where their final interactions occur.
2. In the case of each proton-neutron pair, the momentum and position of both the proton and neutron are adjusted to match the 2-particle rest frame of this pair.
3. The particle that has decoupled at an earlier time is subsequently advanced to the later time of the other particle in the system.
4. The relative momenta $\Delta p = |\overrightarrow{p_1} - \overrightarrow{p_2}|$ and the relative distances $\Delta r = |\overrightarrow{x_1} - \overrightarrow{x_2}|$ are computed for the proton-neutron (p-n) pair in the 2-particle rest frame when their times are equal. The yield of deuteron candidates is determined by satisfying the conditions

$\Delta p < \Delta p_{max}$ and $\Delta r < \Delta r_{max}$. In this particular case, we have set the parameters to $\Delta p_{max} = 0.285$ GeV/c and $\Delta r_{max} = 3.575$ fm.

3.3.2 Triton and helium-3 production

For tritons and helium-3, we use (Hillmann et al., 2022):

1. We examine the two-particle rest frame for every possible two-nucleon pair. If the relative distance between them ($\Delta r = |\overrightarrow{r}_{n_1} - \overrightarrow{r}_{n_2}|$) is less than $\Delta r_{max,nn} = 3.575$ fm, and the momentum distance $\Delta p = |\overrightarrow{p}_{n_1} - \overrightarrow{p}_{n_2}|$ is less than $\Delta p_{max,nn} = 0.285$ GeV/c, it suggests the potential formation of a two-nucleon state. In this case, the combined momenta are represented as $\overrightarrow{p}_{nn} = \overrightarrow{p}_{n_1} + \overrightarrow{p}_{n_2}$, and the position is given by $\overrightarrow{r}_{nn} = \frac{1}{2}(\overrightarrow{r}_{n_1} + \overrightarrow{r}_{n_2})$. These parameters, $\Delta r_{max,nn}$ and $\Delta r_{max,nn}$, align with those previously determined for the deuteron. The subscripts here denote the momentum and position with a given nucleon state.
2. In this step, we transition into the local rest frame of this two-nucleon state and any possible third nucleon. Under the condition that their relative separation ($\Delta r = |\overrightarrow{r}_{nn} - \overrightarrow{r}_{n_3}| < \Delta r_{max,nnn}$) and momentum difference ($\Delta p = |\overrightarrow{p}_{nn} - \overrightarrow{p}_{n_3}| < \Delta p_{max,nnn}$), a triton with a charge of 1 or a helium-3 with a charge of 2 is generated with a likelihood of $\frac{1}{12} \cdot \frac{1}{3!}$. Here, the initial factor corresponds to the spin-isospin coupling, and the subsequent factor accommodates the diverse permutations that produce the same nnn-state. The momentum of the resulting three-nucleon state is then computed as $\overrightarrow{p}_{nnn} = \overrightarrow{p}_{nn} + \overrightarrow{p}_{n_3}$, and the position is determined as $\overrightarrow{r}_{nnn} = \frac{1}{3}(\overrightarrow{r}_{n_1} + \overrightarrow{r}_{n_2} + \overrightarrow{r}_{n_3})$.
3. In the absence of a third particle and in cases where the charge equals 1, the creation of a deuteron is carried out with a probability of $\frac{3}{8} \cdot \frac{1}{2!}$. The initial factor in this probability accounts for the spin-isospin coupling, while the subsequent factor accommodates the various combinations that lead to the same nn-state. This particular treatment for deuterons mirrors the methodology previously described in the citation (Sombun et al., 2019), with the additional factor of $\frac{1}{2!}$ introduced to address the issue of combinatorial double counting in the numerical procedure.

3.3.3 Helium-4 production

The procedures on this nuclear cluster follow the previous steps as mentioned in the previous section on the triton and helium-3 production. However, the coalescence parameter Δr_{ij} and Δp_{ij} were fitted separately to the measurements from the E864 experiment (Armstrong et al., 2000).

In order to provide an agreement between results from the UrQMD simulation model with additional implementations on how nuclear clusters were produced and experimental data, results taken from various experiments as well as the thermal model fit, were included in the comparison. Figure 3.2 displays the beam-energy dependence of the ratios for both d/p and $\bar{d}/\bar{p}$ along with corresponding experimental data. It is obvious to see that the ratios $\frac{d}{p}$ and $\frac{\bar{d}}{\bar{p}}$ are consistently agreed with both the thermal model fit and the experimental data. This agreement supports the validity of the simulation model with the implemented modifications on the nuclear cluster production in coalescence approach.

3.4 UrQMD simulation

For our simulation of heavy-ion collisions, we utilize the UrQMD model, which incorporates a coalescence model for the dynamic formation of nuclei from protons and neutrons with identical momenta and positions. In our simulation, the program was in version 3.4 and we also configured the model to operate in coalescence mode, considering projectile masses corresponding to a mass of 197 (the mass of Au, gold). We conducted a simulation of Au+Au collisions from $t = 1$ fm/c until 40 fm/c across a range of beam energies from $E_{\text{lab}} = 2.0$ AGeV to 3.0 AGeV.

3.5 Data analysis

After the simulation, the outputs of interest are stored in files with the extension ".f13". In contrast to the usual UrQMD output which gives particle vectors only at the freeze-out, we store the complete time evolution of the collisions. On these files, we perform our data analysis by text processing Python code via Jupyter Notebook to extract particle vectors including particle type (itype), coordinate (x,y,z), electric charge. Here the light nuclei: free proton (p), deuteron (d), triton (t), helium-3 (^3He), and helium-4 (^4He) are our particles of interest. After that we count only particles whose coordinates lie within a spatial volume defined as a sphere with 2 fm radius located at origin (0,0,0) and average their multiplicities over the whole set of events for each time step. Then we can plot the time evolution in light nuclei production for given beam energies. We repeat this procedure for cuts in momentum space rather than position space as it is done by experiments.

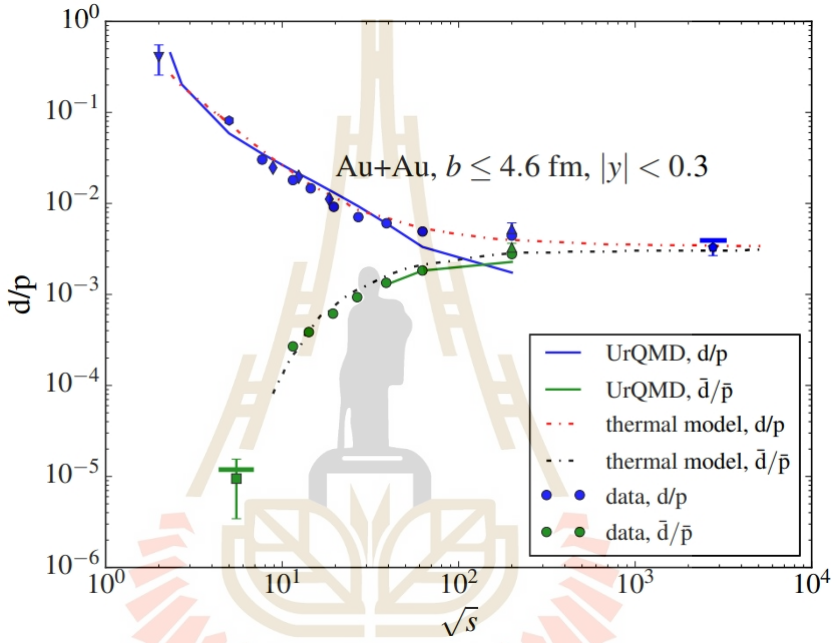

Figure 3.2 Beam-energy dependence of the deuteron to proton ratio from the UrQMD simulation (solid lines), thermal model fit (dotted lines). The symbols of different styles denote the experimental data from the corresponding collaborations: SIS (triangle down), E802 (hexagon), PHENIX (triangles up), NA49 (blue diamonds), STAR (circles), ALICE (pentagon), E814 (square). The blue horizontal line represents the UrQMD+hydro result on the d/p ratio at 2.76 TeV and the green horizontal line represents the UrQMD result of the $\frac{\bar{d}}{\bar{p}}$ ratio in Si+Au collisions at $E_{\text{lab}} = 14.6\ A\text{GeV}$ (Sombun et al., 2019).

3.5.1 Propagation of the light nuclei in coordinate space

As far as we have tracked the position in particle time steps, we need to obtain their positions in the coordinate space (within a spatial volume). The position as a function of time can be expressed as a vector function:

$$\overrightarrow{r}\ (t) = \overrightarrow{r}\ (t_{fr}) + \overrightarrow{v}\ (t_{fr})\Delta t \tag{22}$$

where $\overrightarrow{r}\ (t)$ is the position of the particle at its proper time t, t_{fr} is freeze-out time with $\Delta t = t - t_{fr}$ and $\overrightarrow{v} = \frac{\overrightarrow{p}}{E}$ is the particle's relativistic velocity.

Once the particle positions are obtained, we then proceed to count only the particles that locate within the volume of the sphere i.e., $|\overrightarrow{r}| < 2.0$ fm and continue to perform calculation on their fluctuations.

The next chapter will be presenting the results, where the calculated fluctuations are analyzed and interpreted.

CHAPTER IV

RESULTS AND DISCUSSION

This chapter consists of results from calculations performed during the data analysis, focusing on the outcomes of the model simulation.

4.1 Time evolution in light nuclei multiplicities

After the extraction of the light nuclei in which we are interested in, we can now plot the time evolution of their multiplicities within the spatial volume compared to the multiplicities at midrapidity $|y| < 0.50$ for beam energies of 2.0 AGeV and 3.0 AGeV (see figures 4.1-4.2).

Figure 4.1 presents the time evolution of light nuclei multiplicities at beam energies of 2.0 AGeV (averaged over 64,000 events) and 3.0 AGeV (averaged over 80,000 events). In the early and late stages of the reaction, the multiplicities in both the first-order phase transition and crossover scenarios exhibit minimal differences. However, during the interval corresponding to the co-existence phase, approximately between 8 and 24 fm/c, the average baryon density attained in the first-order phase transition case exceeds that of the crossover. This enhanced density within a fixed central spatial volume leads to an increased net baryon number and yields of the light nuclei within the same region.

On the contrary, the evolution in momentum space shows no differences between the crossover and phase transition scenarios, with yields being almost identical for all examined particle species. This indicates that phase transition primarily influences the spatial configuration of baryons in the dense phase, while having little impact on momentum space fluctuations.

4.2 Time evolution in cumulant ratios of the light nuclei

It is now interesting to explore whether a phase transition has an impact on baryon number fluctuations and, in turn, on correlations in phase space. To investigate this, we study how the cumulant ratios defined in Eq. (13) change over time, beginning with the scaled variance shown in figures 4.3 and 4.4 for beam energies of $E_{\text{lab}} = 2.0$ AGeV and 3.0 AGeV (top and bottom panels, respectively).

In coordinate space, we observe that the total baryon number remains conserved, causing the baryon values to start below the Poisson baseline of 1, in contrast to other particles. A significant increase in $\frac{\sigma^2}{\mu}$ is found in the phase transition scenario compared to the crossover, peaking at the moment of maximum compression. Protons exhibit a less pronounced increase, they constitute only a fraction of the total baryon number and are subject to resonance excitations and decays. Nuclear clusters show an even smaller but still noticeable enhancement.

Proceeding to the evolution in the momentum space, minimal differences between the crossover and phase transition scenarios are observed, with particle yields of all species remaining nearly identical. This indicates that phase separation primarily influences the spatial distribution of baryons in the dense phase, while having only a minor impact on fluctuations in the momentum space.

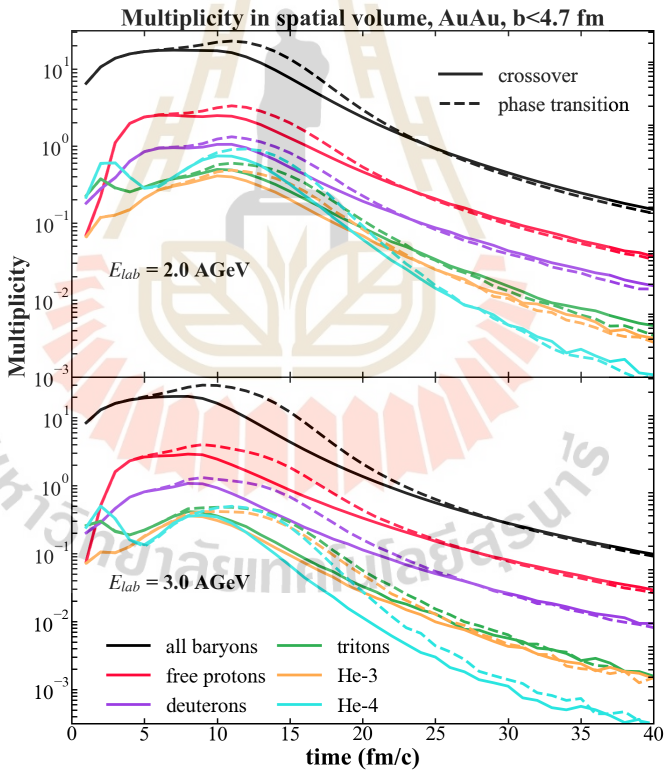

Figure 4.1 Time evolution in light nuclei multiplicities (proton (red), deuteron (purple), triton (green), ^3He (orange), ^4He (blue) at $E_{\text{lab}} = 2.0$ AGeV (upper plot) and 3.0 AGeV (lower plot). The plots display the multiplicities within the spherical volume with radius 2 fm centered at the origin from UrQMD calculations with phase transition (dashed lines) and with a crossover (solid lines).

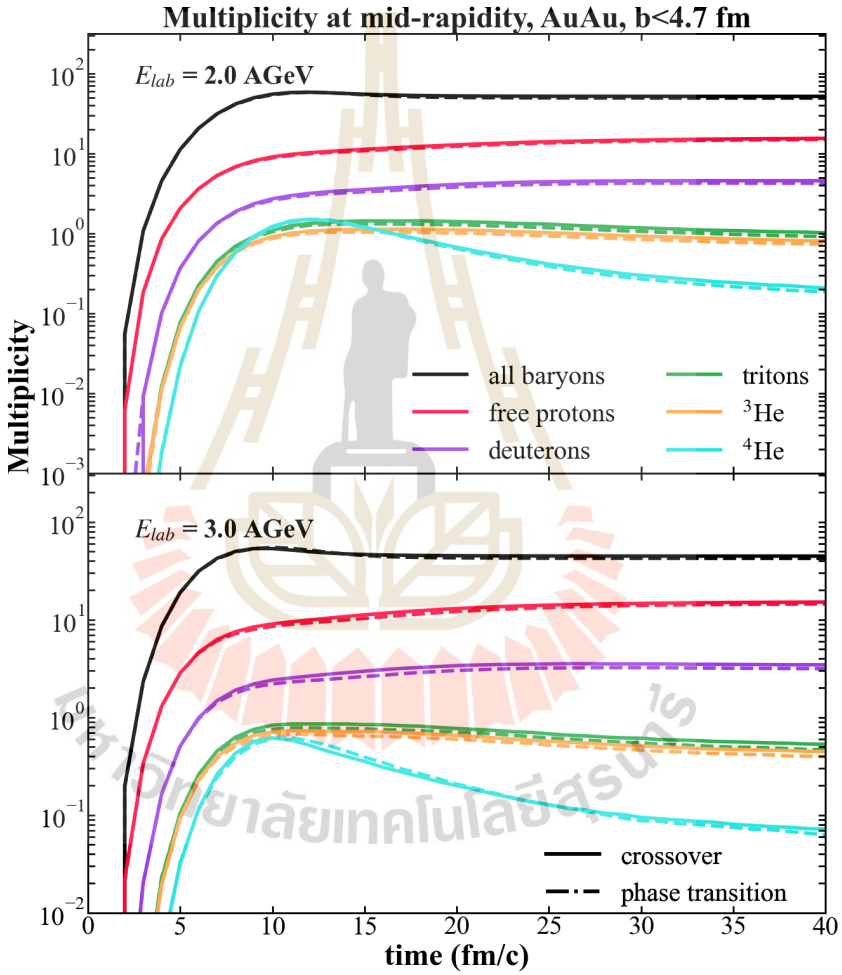

Figure 4.2 Time evolution in light nuclei multiplicities (proton (red), deuteron (purple), triton (green), ^3He (orange), ^4He (blue) at $E_{\text{lab}} = 2.0$ AGeV (upper plot) and 3.0 AGeV (lower plot). The plots display the multiplicities at mid-rapidity $|y| \leq 0.5$ from the same calculations.

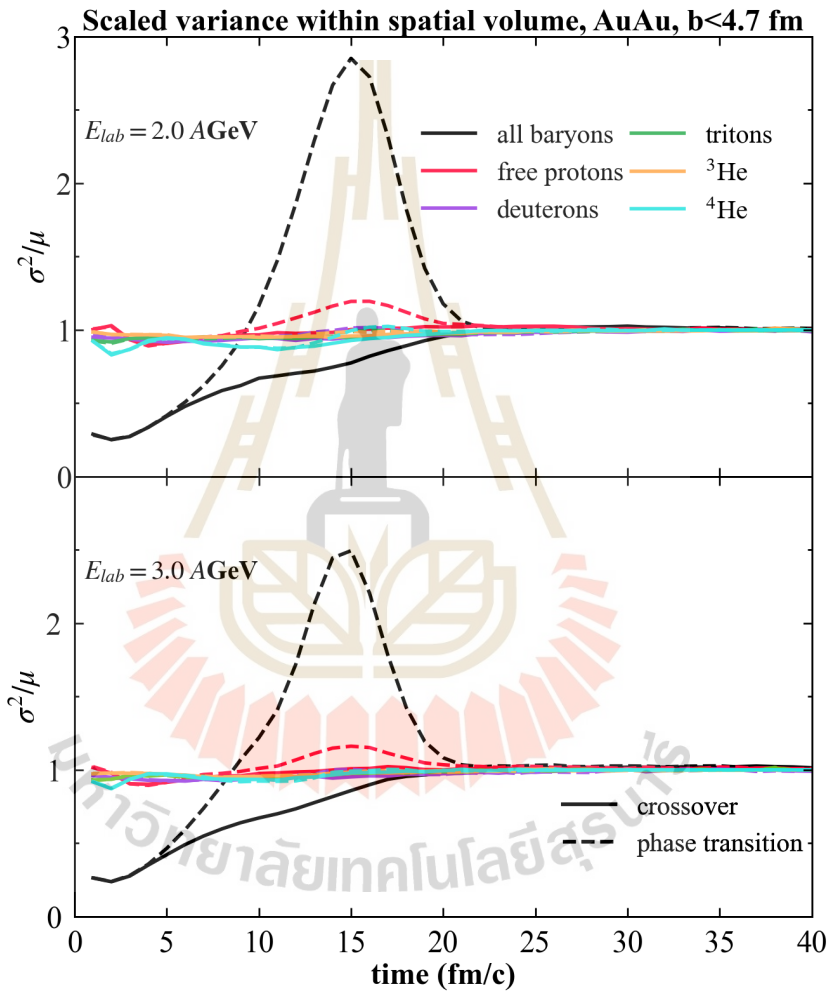

Figure 4.3 Time evolution of the scaled variance of the multiplicities of baryons (grey), protons (red) and light nuclei (deuterons (purple), tritons (green), ^3He (orange), ^4He (blue)) at $E_{\text{lab}} = 2.0$ AGeV (upper plot) and 3.0 AGeV (lower plot) within a spatial volume. The UrQMD calculations were carried out using a CMF equation of state (EoS) that includes either a first-order phase transition (dashed lines) or a smooth crossover (solid lines). A distinct enhancement in the baryon cumulants is observed during the phase transition.

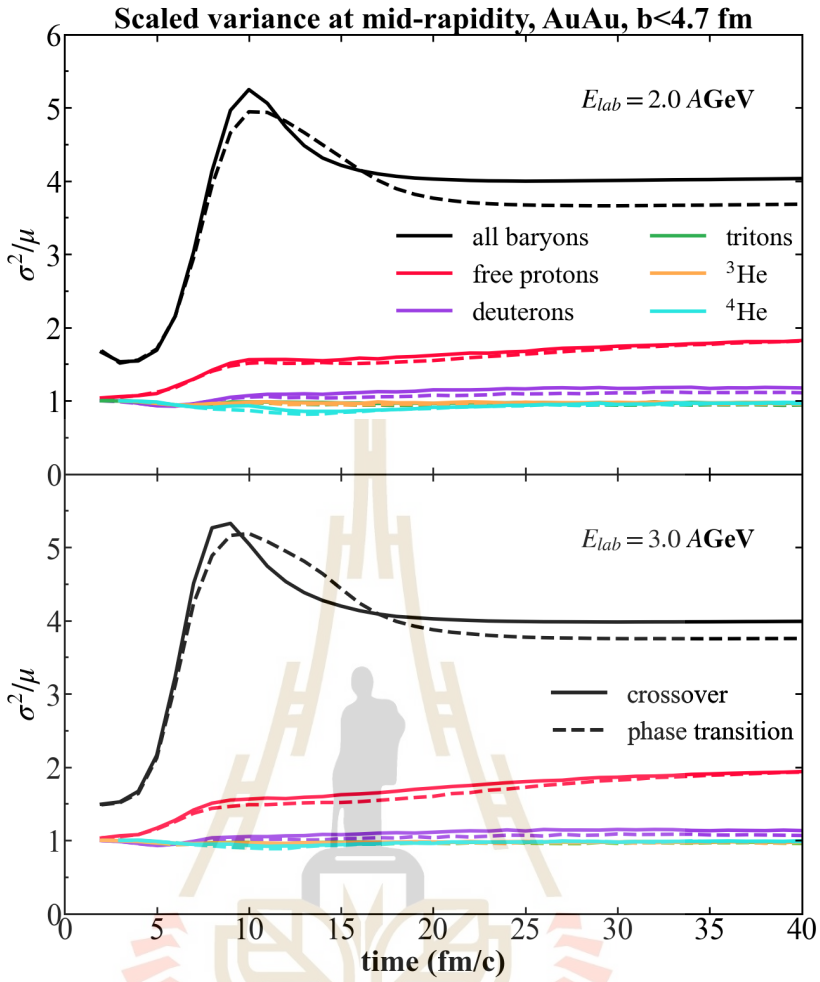

Figure 4.4 Time evolution of the scaled variance of the multiplicities of baryons (grey), protons (red) and light nuclei (deuterons (purple), tritons (green), ^3He (orange), ^4He (blue)) at $E_{\text{lab}} = 2.0$ AGeV (upper plot) and 3.0 AGeV (lower plot) within the rapidity interval $-0.50 \leq y \leq 0.50$ from the same UrQMD calculations with the phase transition EoS. During the phase transition, free protons and other nuclear clusters are only slightly affected.

The behavior of $S\sigma$ shows a similar tendency, as displayed in figure 4.5. However, a clear discrimination appears at higher energy of $E_{\text{lab}} = 3.0\ A\text{GeV}$, particularly in the lower plot. At this energy, the presence of a phase transition results in a pattern of enhancements, followed by suppression, and then another enhancement in the net-baryon number cumulant, conversely to the smoother behavior seen with a crossover. This pattern arises from the qualitatively different dynamical evolution of the system at two energies. Explicitly, at $E_{\text{lab}} = 3.0\ A\text{GeV}$, the system overshoots into the spinodal region while crossing spinodal lines during its expansion which is not a feature observed at the lower energy.

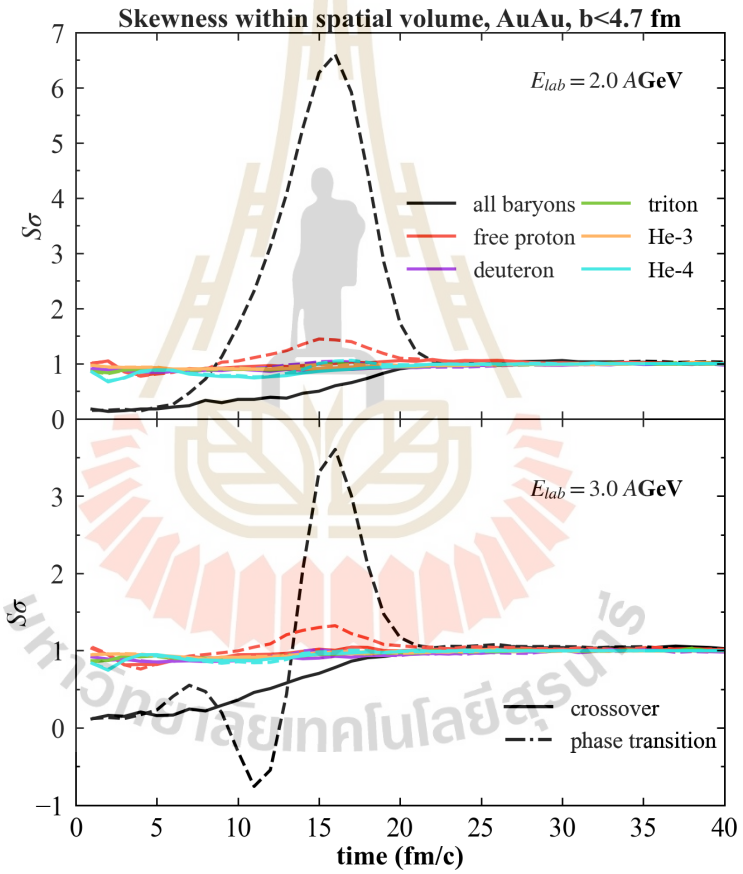

Figure 4.5 Time evolution of the skewness of the multiplicities of baryons (black), protons (red) and light nuclei (deuterons (purple), tritons (green), ^3He (orange), ^4He) at $E_{\text{lab}} = 2.0\ A\text{GeV}$ (upper plot) and $3.0\ A\text{GeV}$ (lower plot). The plots show the results within a spatial volume. UrQMD calculations were conducted using a CMF EoS incorporating either a first-order phase transition (dashed lines) or a smooth crossover (solid lines).

Correspondingly to the scaled variance, the evolution in momentum space of $S\sigma$ does not exhibit a clear distinction between the two scenarios. Although a late-time suppression of $S\sigma$ is also observed at 2.0 AGeV, the effect is considerably weaker at 3.0 AGeV (see figure 4.6). This aligns with previous findings indicating that volume fluctuations have a greater impact on second-order cumulants than on third-order ones (Bzdak, Koch and Skokov, 2017).

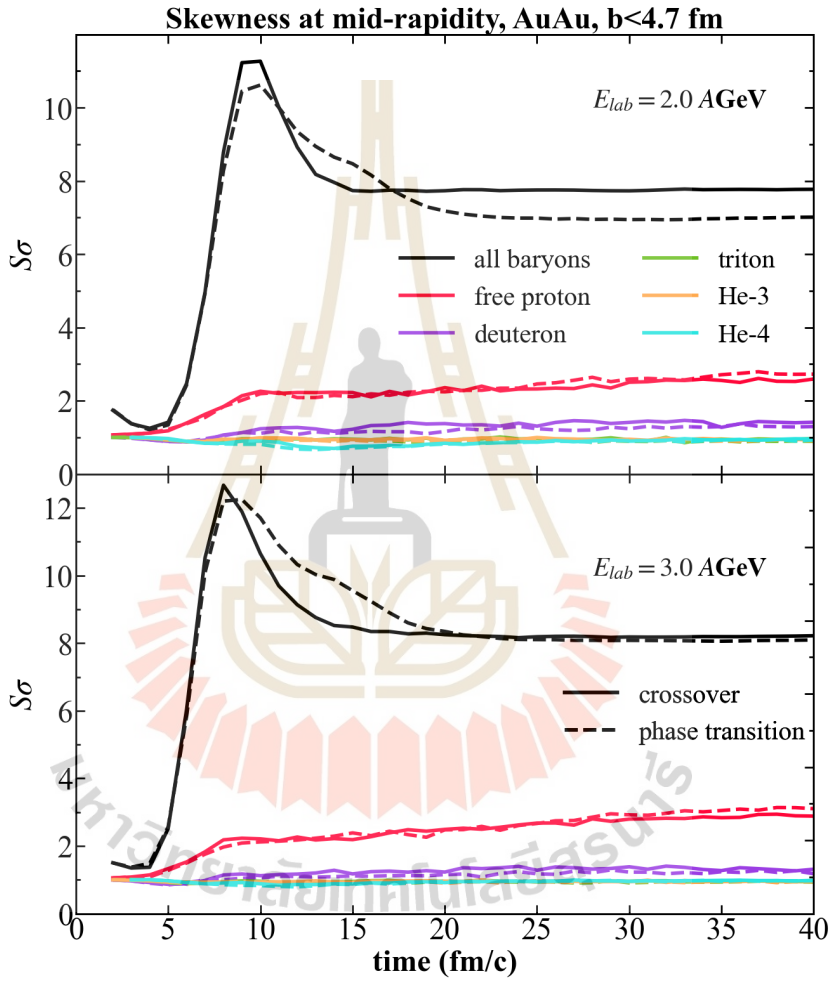

Figure 4.6 Time evolution of the skewness of the multiplicities of baryons (black), protons (red) and light nuclei (deuterons (purple), tritons (green), ^3He (orange), ^4He) at $E_{\text{lab}} = 2.0$ AGeV (upper plot) and 3.0 AGeV (lower plot). The plots show the results within the rapidity range $|y| \leq 0.50$ from the same UrQMD calculations with the phase transition EoS.

4.3 Cumulant ratios in different rapidity windows

Although no significant signal is observed in the momentum space, it remains crucial to determine the optimal choice of rapidity acceptance window for experimentally studying cumulant ratios. Therefore, we examine how the cumulants for baryons, deuterons, and free protons vary with the width of the rapidity window.

The rapidity window is defined by $\Delta y = y_{max} - y_{min}$ where y_{max} and y_{min} are maximum and minimum rapidity, respectively, with $y_{min} = -y_{max}$ and $y_{max} > 0$. We have chosen rapidity windows at two fixed time steps of 8 fm/c and 50 fm/c to compare fluctuations in the initial and late stage of the collision for the corresponding cumulant ratios: the scaled variance $\frac{\sigma^2}{\mu}$ which is available in figures 4.7-4.10 and the skewness $S\sigma$ (see figures 4.11-4.14).

Starting with the scaled variance, the largest baryon fluctuations are observed around $\Delta y = 1.0$, for very narrow windows, the fluctuations become Poissonian, and for the wide windows, conservation of baryon number contributes the prominent role. For the rest of the nuclear clusters i.e., proton, deuteron, triton, helium-3, and helium-4, one can observe a slight difference between two scenarios with the crossover having stronger effects. Overall, the proton number fluctuates less than the baryon number, as one might perceive, along with the slight differences between the two scenarios can be seen for the rest of the nuclear clusters which are not involved as a significant signal.

Next, we proceed to the skewness. Although the effects of the scaled variance which include participant fluctuations are prominently in active for all rapidity windows, we cannot observe explicit enhancements in the skewness of the free protons as well as the nuclear clusters in case of a phase transition for larger rapidity windows. Therefore, we propose that the skewness in a rapidity window of $\Delta y = 1.0$ is the most appropriate to observe any signals of a phase transition provided here.

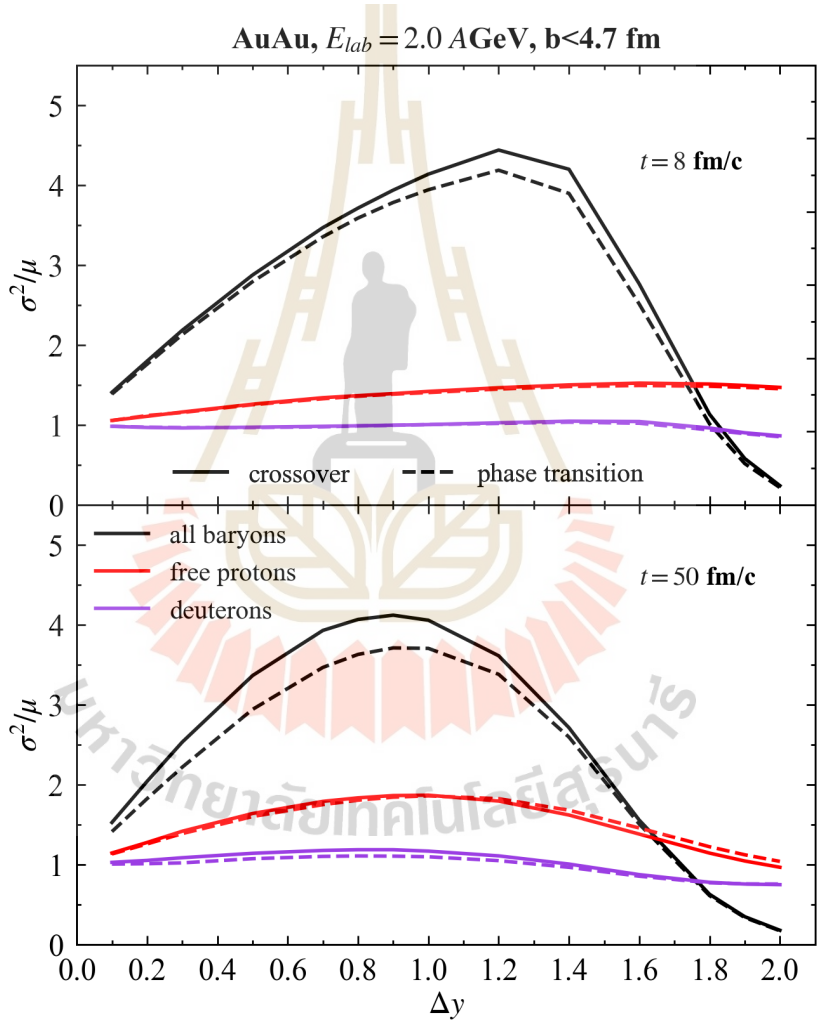

Figure 4.7 Scaled variance as a function of rapidity window of the baryons (black), protons (red) and deuterons (purple) at the time 8 fm/c and 50 fm/c $E_{\text{lab}} = 2.0$ AGeV

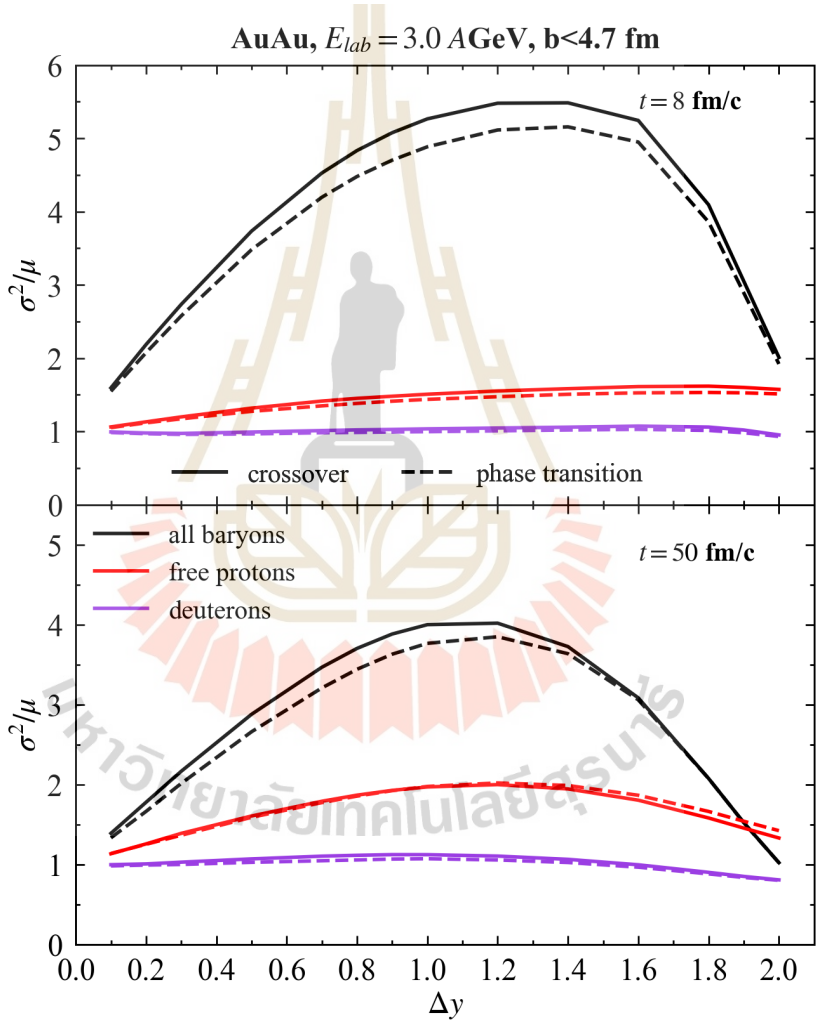

Figure 4.8 Scaled variance as a function of rapidity window of the baryons (black), protons (red) and deuterons (purple) at the time 8 fm/c and 50 fm/c $E_{\text{lab}} = 3.0$ AGeV

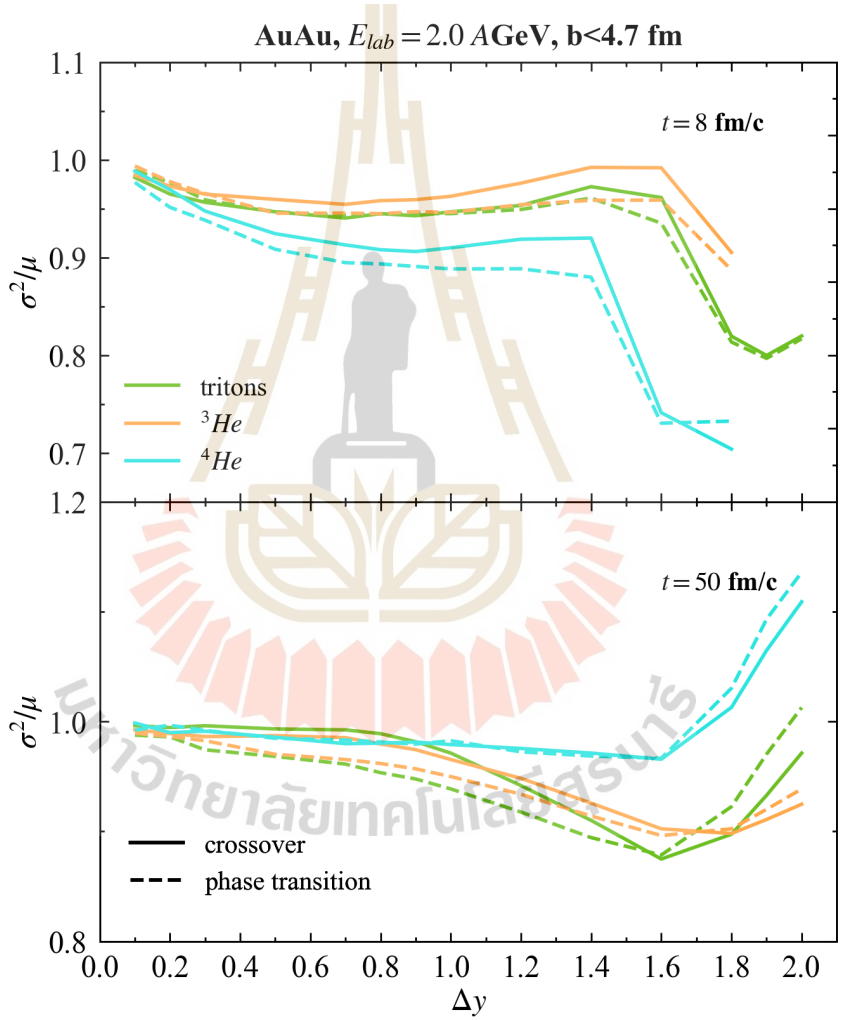

Figure 4.9 Scaled variance as a function of rapidity window of tritons (green), ^3He (orange) and ^4He (blue) at the time 8 fm/c and 50 fm/c $E_{\text{lab}} = 2.0$ AGeV

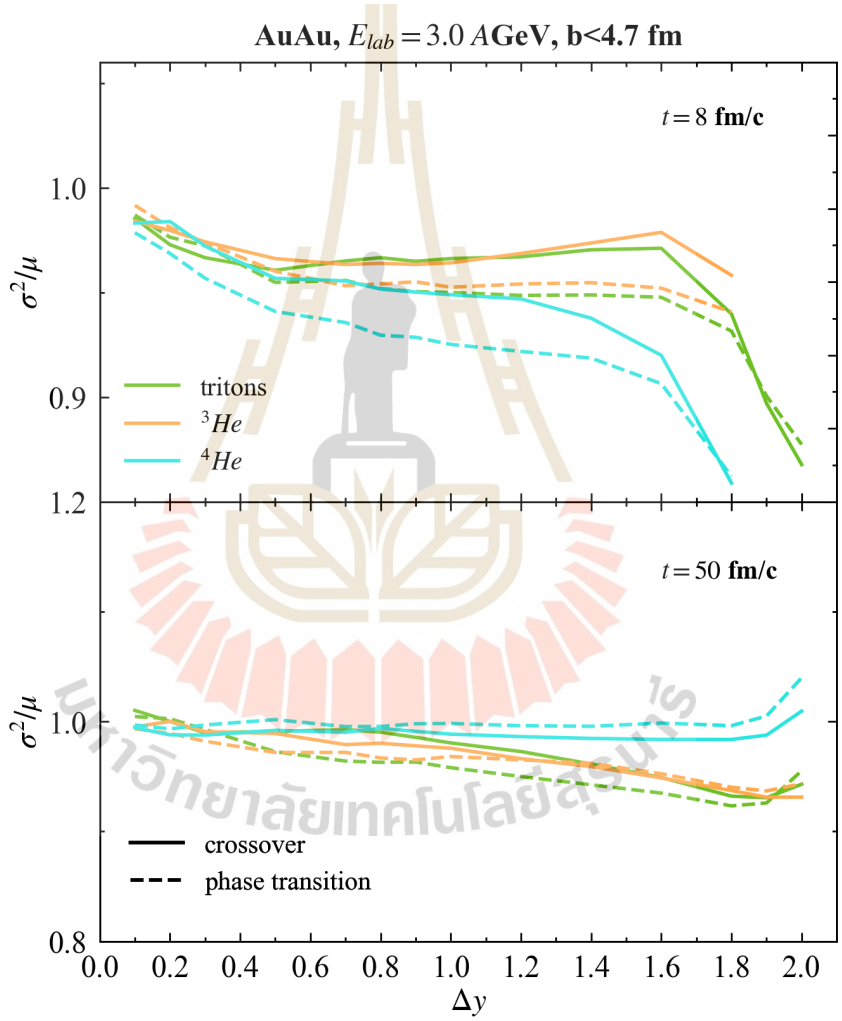

Figure 4.10 Scaled variance as a function of rapidity window of tritons (green), ^3He (orange) and ^4He (blue) at the time 8 fm/c and 50 fm/c $E_{\text{lab}} = 3.0$ AGeV

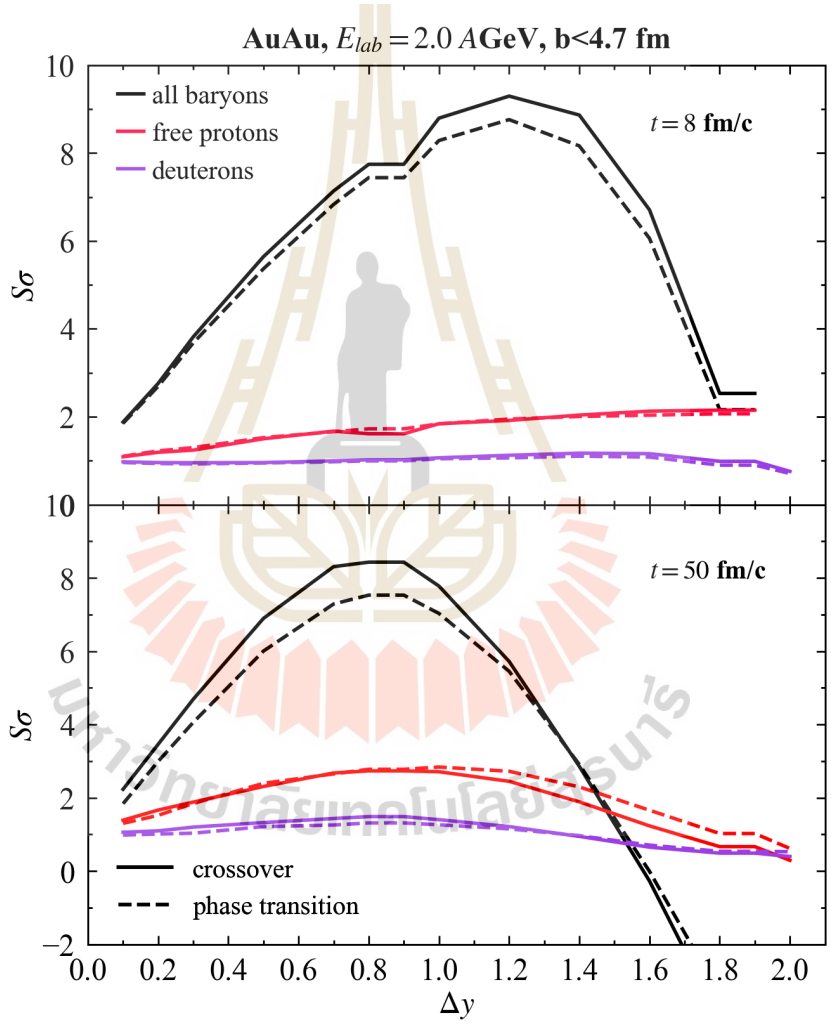

Figure 4.11 $S\sigma$ as a function of rapidity window of the baryons (black), protons (red) and deuterons (purple) at the time 8 fm/c and 50 fm/c $E_{\text{lab}} = 2.0$ AGeV

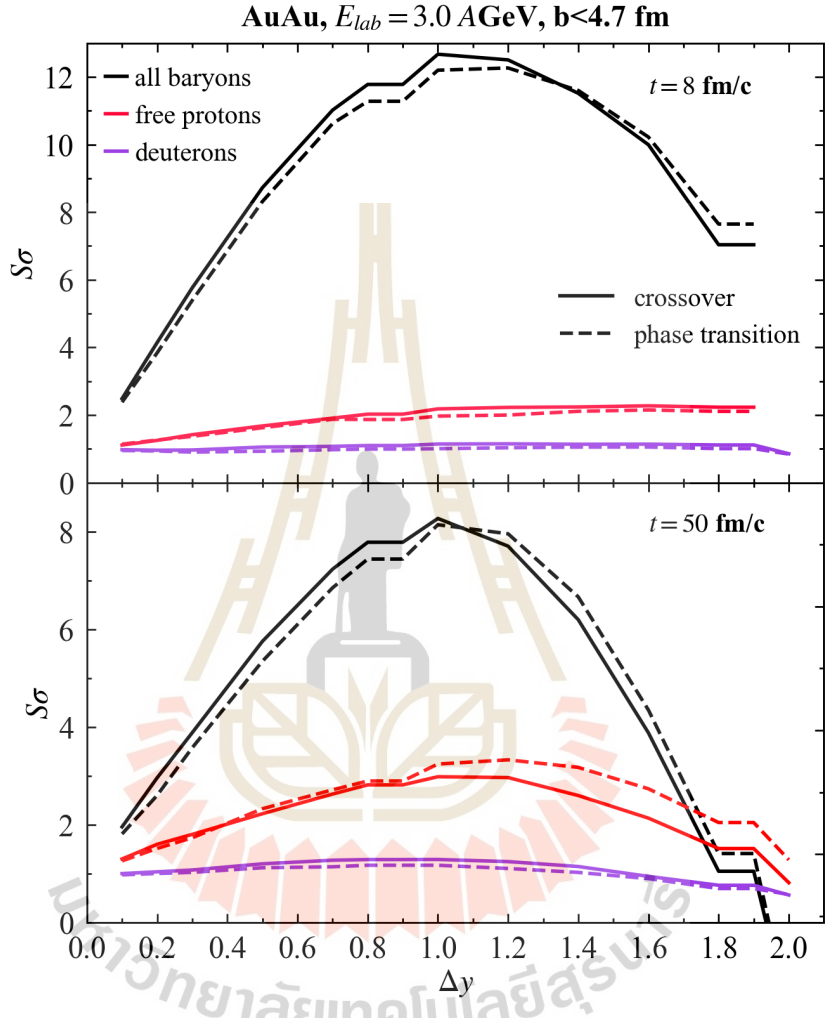

Figure 4.12 $S\sigma$ as a function of rapidity window of the baryons (black), protons (red) and deuterons (purple) at the time 8 fm/c and 50 fm/c $E_{\text{lab}} = 3.0$ AGeV

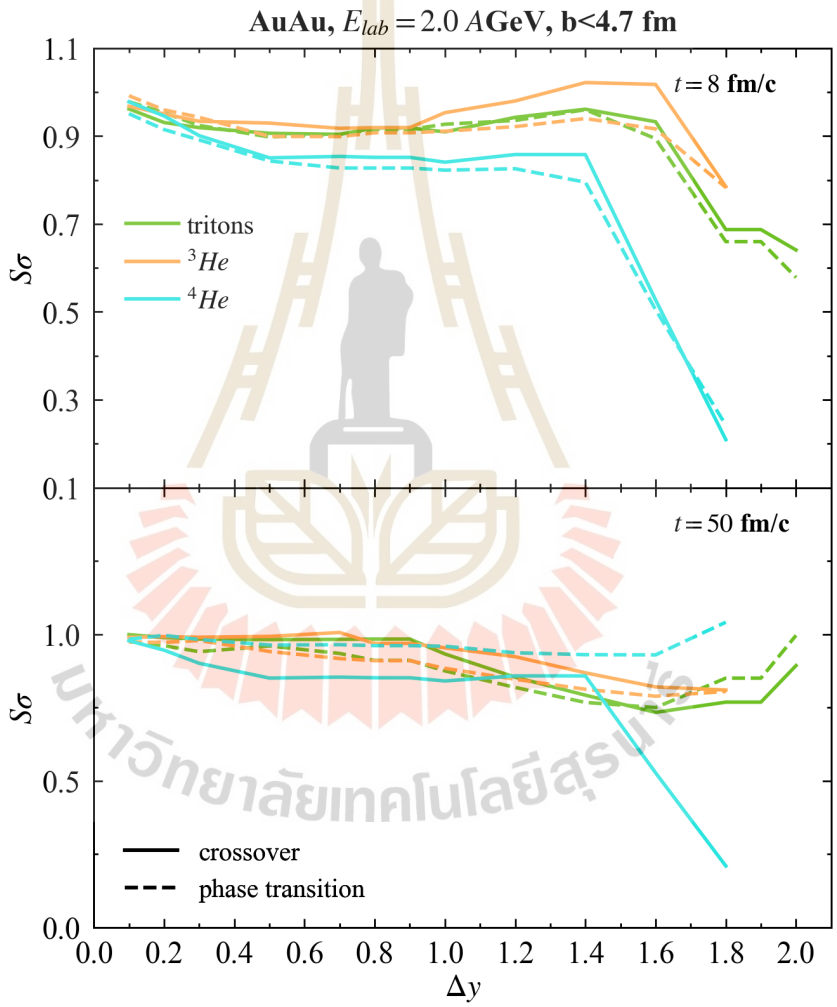

Figure 4.13 $S\sigma$ as a function of rapidity window of tritons (green), ^3He (orange) and ^4He (blue) at the time 8 fm/c and 50 fm/c $E_{\text{lab}} = 2.0$ AGeV

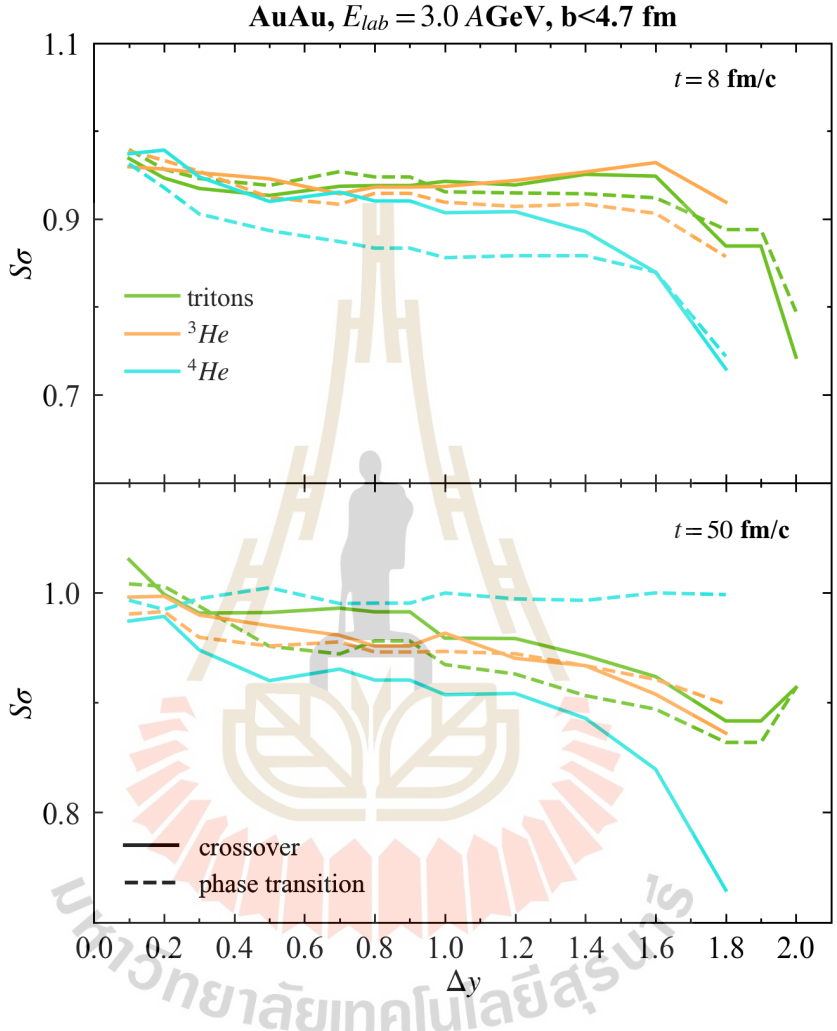

Figure 4.14 $S\sigma$ as a function of rapidity window of tritons (green), ^3He (orange) and ^4He (blue) at the time 8 fm/c and 50 fm/c $E_{\text{lab}} = 3.0$ AGeV

After we are done observing the results with the rapidity window dependence, the upcoming section is going to represent how we confirm our calculations according to experimental data in a picture of actual collision picture via time evolution in light nuclei ratios.

4.4 Light nuclei ratios

After the comparison between the fluctuations in different rapidity windows, we can now treat the results as a confirmation that the phase transition will have a substantial impact to fluctuations of the baryon number in coordinate space (spatial volume). We can calculate the time dependence in the double ratios between the following particles: proton (p), deuteron (d), triton (t), helium-3 (^3He), and helium-4 (^4He). The double ratios are expressed as (STAR Collaboration, 2023)

$$\frac{(t)(p)}{d^2} \text{ and } \frac{(^4He)(p)}{(^3He)(d)} . \tag{23}$$

These expressions in double ratios are useful since they eliminate the volume factor as the number of a certain nuclear cluster is calculated using the thermal model. Figures 4.15 and 4.16 display the time evolution in the ratios for corresponding beam energies in comparison between the results from coordinate space and momentum space.

For every curve, we observe that the ratios begin to rise until about 10 fm/c, at which point a minor enhancement in the phase transition over the crossover occurs. Remarkably, for both examined beam energies, this is also readily apparent in the ratio $(N_{^4He} \times N_p)/(N_{^3He} \times N_d)$ determined in the rapidity window. In contrast, the cumulant ratio never displayed a distinct signal in momentum space. But all ratios eventually become close to the same value after a long enough period of time. The double ratios are also compared to the STAR experiment results at $E_{\text{lab}} = 3.0\ A\text{GeV}$ (Abdulhamid et al., 2024) for completeness, and correspond well with the values obtained from our models for both equations of state at late times. In agreement with this, experimentally we can only observe these ratios at late times. Any peak structure or sudden modification is not visible due to the absence of further interactions as the system reaches its freeze-out state.

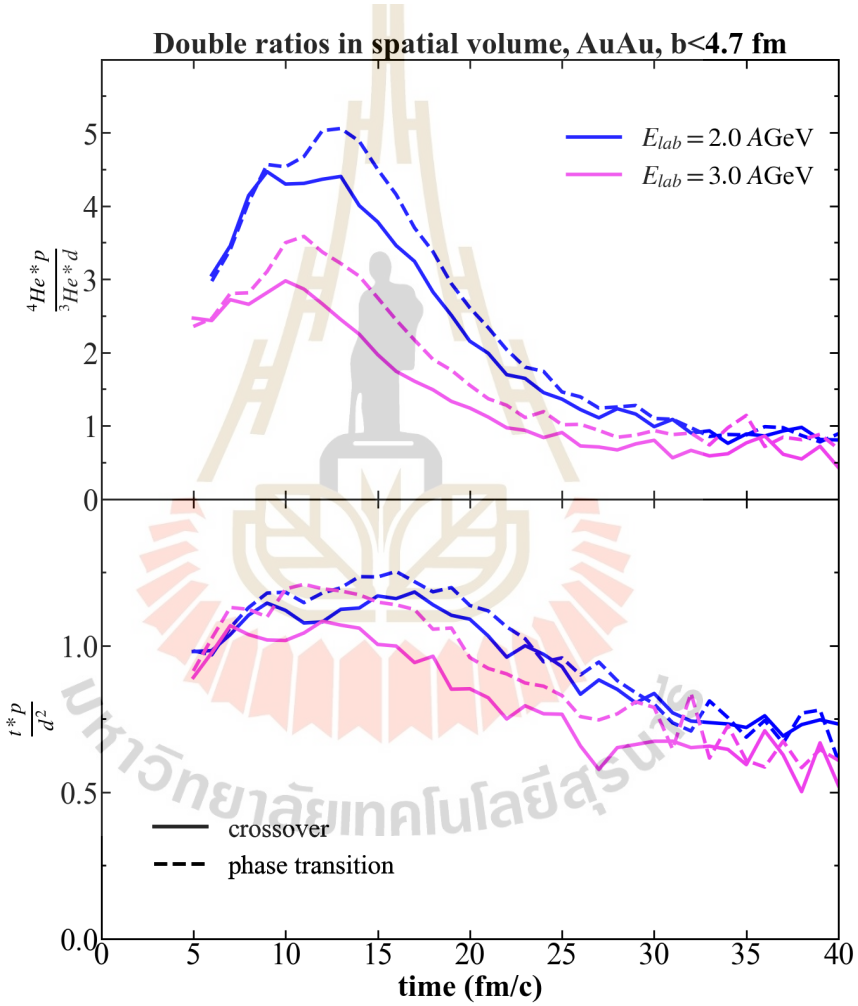

Figure 4.15 Time evolution of double ratios $\frac{(t)(p)}{d^2}$ and $\frac{(He4)(p)}{(He3)(d)}$ for corresponding energies of $2.0\ A$GeV (blue) and $3.0\ A$GeV (pink) in coordinate space.

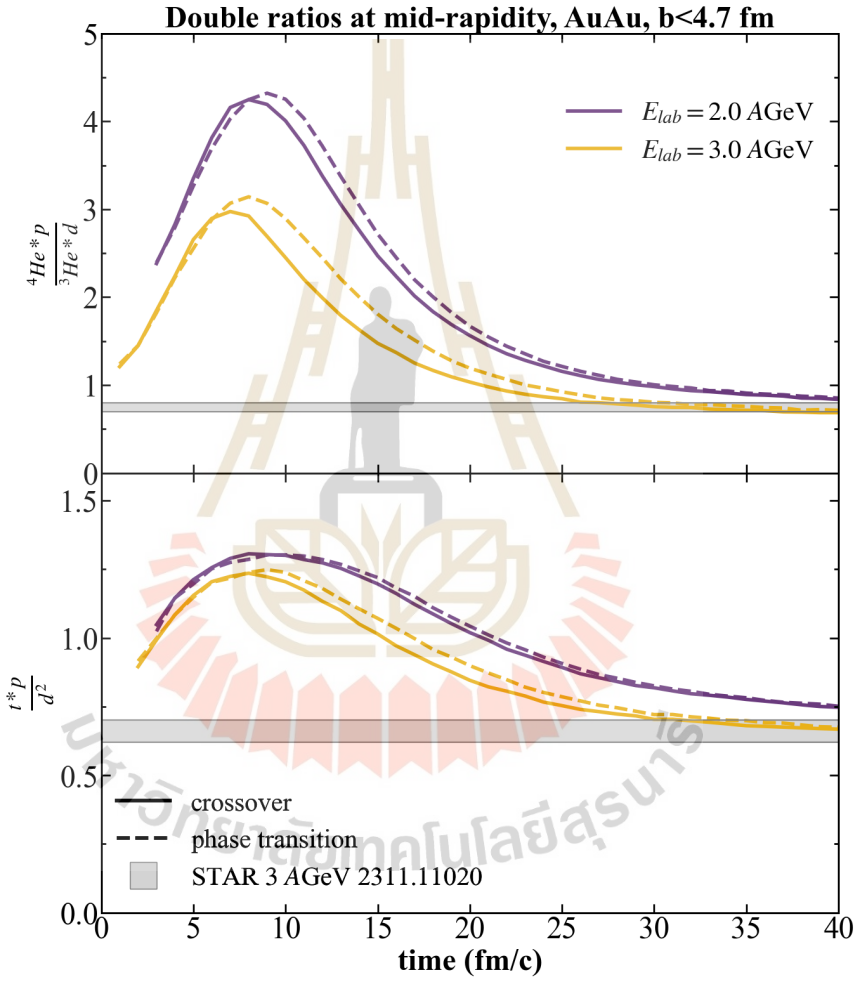

Figure 4.16 Time evolution of double ratios $(t * p)/d^2$ and $(^4He * p)/(^3He * d)$ for corresponding energies of 2.0 AGeV (purple) and 3.0 AGeV (yellow) in momentum space. The gray bands correspond to the results from the STAR experiment of Au+Au at $E_{\text{lab}} = 3.0$ AGeV, $0 - 10\%$ centrality. The data is taken from figure 16 (b) in (Abdulhamid et al., 2024).

CHAPTER V

CONCLUSION

In conclusion, our research involves simulating light nuclei formation using UrQMD and conducting a series of data analyses. We begin by examining double ratios for the relevant light nuclei, followed by calculating the time evolution of proton number skewness and scaled variance along with their ratios (susceptibilities). Subsequently, we determine time-dependent proton number cumulants. The phase transition is influenced by the enhancements in the production of the baryons and the light nuclei at low beam energies. Our analysis covered the time evolution of these observables in both coordinate and momentum space, with the latter being particularly pertinent for experimental observations.

Overall, our findings within a central spherical volume consistently demonstrate that a strong first-order phase transition significantly alters the corresponding observables compared to a crossover scenario. The most pronounced changes were observed in the cumulant ratios σ^2/μ and $S\sigma$ of the net-baryon number.

For experimentally measurable proton number cumulants, the higher-order cumulants of free protons evaluated over wide rapidity windows ($\Delta y > 1$) show the greatest potential as sensitive observables.

Within a rapidity window of $\Delta y = 1$, the only notably distinct and potentially useful effect in light nuclei production was observed in the ratio $(N_{^4He} \times N_p)/(N_{^3He} \times N_d)$, which showed an approximately 10% enhancement at intermediate times. However, the signal weakens at later stages, decreasing the probability of detection in experiments.

REFERENCES

REFERENCES

Abdallah, M. S., Adam, J., Adamczyk, L., Adams, J. R., Adkins, J. K., Agakishiev, G., Aggarwal, I., Aggarwal, M. M., Ahammed, Z., Alekseev, I., Anderson, D. M., Aparin, A., Aschenauer, E. C., Ashraf, M. U., Atetalla, F. G., et al. (2025). Erratum: Cumulants and correlation functions of net-proton, proton, and antiproton multiplicity distributions in Au + Au collisions at energies available at the BNL Relativistic Heavy Ion Collider [Phys. Rev. C 104, 024902 (2021)]. *Phys. Rev. C 111*, 029902.

Abdulhamid, M. I., Aboona, B. E., Adam, J., Adamczyk, L., Adams, J. R., Aggarwal, I., Aggarwal, M. M., Ahammed, Z., Aschenauer, E. C., Aslam, S., Atchison, J., Bairathi, V., Cap, J. G. B., Barish, K., Bellwied, R., et al. (2024). Production of protons and light nuclei in Au + Au collisions at $\sqrt{s_{NN}} = 3$ GeV with the STAR detector. *Phys. Rev. C 110*, 054911.

Adamczewski-Musch, J., Arnold, O., Behnke, C., Belounnas, A., Belyaev, A., Berger-Chen, J. C., Blanco, A., Blume, C., Böhmer, M., Bordalo, P., Chernenko, S., Chlad, L., Ciepał, I., Deveaux, C., Dreyer, J., et al. (2020). Proton-number fluctuations in $\sqrt{s_{NN}} = 2.4$ GeV Au + Au collisions studied with the High-Acceptance DiElectron Spectrometer (HADES). *Phys. Rev. C 102*, 024914.

Aichelin, J. and Stoecker, H. (1986). Quantum molecular dynamics. A Novel approach to N body correlations in heavy ion collisions. *Phys. Lett. B 176*, 14–19.

Albright, M., Kapusta, J. and Young, C. (2015). Baryon number fluctuations from a crossover equation of state compared to heavy-ion collision measurements in the beam energy range $\sqrt{s_{NN}} = 7.7$ to 200 GeV. *Phys. Rev. C 92*, 044904.

Andronov, E. (2019). Search for the critical point by the NA61/SHINE experiment. *Nucl. Phys. A 982*. Ed. by F. Antinori, A. Dainese, P. Giubellino, V. Greco, M. P. Lombardo and E. Scomparin, 835–838.

Aoki, Y., Endrodi, G., Fodor, Z., Katz, S. D. and Szabo, K. K. (2006). The Order of the quantum chromodynamics transition predicted by the standard model of particle physics. *Nature 443*, 675–678.

Armstrong, T. A., Barish, K. N., Batsouli, S., Bennett, S. J., Bertaina, M., Chikanian, A., Coe, S. D., Cormier, T. M., Davies, R., Dover, C. B., Fachini, P., Fadem, B., Finch, L. E., George, N. K., Greene, S. V., et al. (2000). Measurements of light nuclei production in $11.5A\text{GeV}/c$ Au+Pb heavy-ion collisions. *Phys. Rev. C 61*, 064908.

Bass, S., Belkacem, M., Bleicher, M., Brandstetter, M., Bravina, L., Ernst, C., Gerland, L., Hofmann, M., Hofmann, S., Konopka, J., Mao, G., Neise, L., Soff, S., Spieles, C., Weber, H., et al. (1998). Microscopic models for ultrarelativistic heavy ion collisions. *Progress in Particle and Nuclear Physics 41*, 255–369.

Bazavov, A., Bollweg, D., Ding, H.-T., Enns, P., Goswami, J., Hegde, P., Kaczmarek, O., Karsch, F., Larsen, R., Mukherjee, S., Ohno, H., Petreczky, P., Schmidt, C., Sharma, S. and Steinbrecher, P. (2020). Skewness, kurtosis, and the fifth and sixth order cumulants of net baryon-number distributions from lattice QCD confront high-statistics STAR data. *Phys. Rev. D 101*, 074502.

Bhattacharyya, S., Jaiswal, A. and Roy, S. (2021). Chemical freeze-out systematics of thermal model analysis using hadron yield ratios. *103*(2), 024905, 024905.

Biswas, D. (2020). Formation of light nuclei at chemical freezeout: Description within a statistical thermal model. *102*(5), 054902, 054902.

Bleicher, M., Zabrodin, E., Spieles, C., Bass, S. A., Ernst, C., Soff, S., Bravina, L., Belkacem, M., Weber, H., Stöcker, H. and Greiner, W. (1999). Relativistic hadron-hadron collisions in the ultra-relativistic quantum molecular dynamics model. *Journal of Physics G Nuclear Physics 25*(9), 1859–1896.

Braun-Munzinger, P. and Dönigus, B. (2019). Loosely-bound objects produced in nuclear collisions at the LHC. *Nuclear Physics A 987*.

Bumnedpan, T., Steinheimer, J., Bleicher, M., Limphirat, A. and Herold, C. (2022). Enhanced pion-to-proton ratio at the onset of the QCD phase transition. *Physics Letters B 835*, 137537.

Bumnedpan, T., Steinheimer, J., Reichert, T., Herold, C., Limphirat, A. and Bleicher, M. (2025). Time evolution of light nuclei cumulants and ratios with a first-order phase transition in the UrQMD transport model. *Phys. Rev. C 111*, 034910.

Bzdak, A. and Koch, V. (2019). Mapping the QCD phase diagram with statistics-friendly distributions. *100*(5), 051902, 051902.

Bzdak, A., Koch, V. and Skokov, V. (2017). Correlated stopping, proton clusters and higher order proton cumulants. *Eur. Phys. J. C 77*(5), 288.

Dover, C. B., Heinz, U., Schnedermann, E. and Zimányi, J. (1991). Covariant coalescence model for relativistically expanding systems. *Phys. Rev. C 44*, 1636–1654.

Fischer, C. S., Luecker, J. and Welzbacher, C. A. (2014). Phase structure of three and four flavor QCD. *Phys. Rev. D 90*(3), 034022.

Fukushima, K. (2008). Phase diagrams in the three-flavor Nambu-Jona-Lasinio model with the Polyakov loop. *Phys. Rev. D 77*. [Erratum: Phys.Rev.D 78, 039902 (2008)], 114028.

Gao, F. and Pawlowski, J. M. (2021). Chiral phase structure and critical end point in QCD. *Phys. Lett. B 820*, 136584.

Grebieszkow, K. (2009). Search for the critical point of strongly interacting matter in NA49. *Nucl. Phys. A 830*. Ed. by P. Stankus, D. Silvermyr, S. Sorensen and V. Greene, 547C–550C.

Hartnack, C., Li, Z. X., Neise, L., Peilert, G., Rosenhauer, A., Sorge, H., Stoecker, H., Greiner, W. and Aichelin, J. (1989). Quantum Molecular Dynamics: A Microscopic Model From Unilac to CERN Energies. *Nucl. Phys. A 495*. Ed. by W. Cassing and U. Mosel, 303C–320C.

Herold, C., Kittiratpattana, A., Kobdaj, C., Limphirat, A., Yan, Y., Nahrgang, M., Steinheimer, J. and Bleicher, M. (2019). Entropy production and reheating at the chiral phase transition. *Physics Letters B 790*, 557–562.

Herold, C., Nahrgang, M., Mishustin, I. and Bleicher, M. (2014). Formation of droplets with high baryon density at the QCD phase transition in expanding matter. *Nucl. Phys. A 925*, 14–24.

Hillmann, P., Käfer, K., Steinheimer, J., Vovchenko, V. and Bleicher, M. (2022). Coalescence, the thermal model and multi-fragmentation: the energy and volume dependence of light nuclei production in heavy ion collisions. *J. Phys. G 49*(5), 055107.

Huth, S., Pang, P. T. H., Tews, I., Dietrich, T., Le Fèvre, A., Schwenk, A., Trautmann, W., Agarwal, K., Bulla, M., Coughlin, M. W. and Van Den Broeck, C. (2022). Constraining neutron-star matter with microscopic and macroscopic collisions. *606*(7913), 276–280.

Karsch, F. (2017). Lattice QCD results on cumulant ratios at freeze-out. *Journal of Physics: Conference Series 779*(1), 012015.

Kuznietsov, V. A., Gorenstein, M. I., Koch, V. and Vovchenko, V. (2024). Coordinate versus momentum cuts and effects of collective flow on critical fluctuations. *Phys. Rev. C 110*, 015206.

Luo, X. and Nonaka, T. (2019). Efficiency correction for cumulants of multiplicity distributions based on track-by-track efficiency. *Phys. Rev. C 99*, 044917.

Omana Kuttan, M., Motornenko, A., Steinheimer, J., Stoecker, H., Nara, Y. and Bleicher, M. (2022). A chiral mean-field equation-of-state in UrQMD: effects on the heavy ion compression stage. *Eur. Phys. J. C 82*(5), 427.

Sasaki, C., Friman, B. and Redlich, K. (2007). Exploring the QCD phase structure with density fluctuations. *arXiv e-prints*, arXiv:0709.2487, arXiv:0709.2487.

Savchuk, O., Poberezhnyuk, R. V., Motornenko, A., Steinheimer, J., Gorenstein, M. I. and Vovchenko, V. (2023). Phase transition amplification of proton number fluctuations in nuclear collisions from a transport model approach. *Phys. Rev. C 107*, 024913.

Scavenius, O., Mocsy, A., Mishustin, I. N. and Rischke, D. H. (2001). Chiral phase transition within effective models with constituent quarks. *Phys. Rev. C 64*, 045202.

Schaefer, B.-J. and Wambach, J. (2005). The Phase diagram of the quark meson model. *Nucl. Phys. A 757*, 479–492.

Skokov, V., Friman, B. and Redlich, K. (2013). Volume fluctuations and higher-order cumulants of the net baryon number. *Phys. Rev. C 88*, 034911.

Sombun, S., Tomuang, K., Limphirat, A., Hillmann, P., Herold, C., Steinheimer, J., Yan, Y. and Bleicher, M. (2019). Deuteron production from phase-space coalescence in the UrQMD approach. *Phys. Rev. C 99*(1), 014901.

STAR Collaboration (2023). Collision-energy Dependence of Deuteron Cumulants and Proton-deuteron Correlations in Au+Au collisions at RHIC. https://doi.org/10.48550/arXiv.2304.10993.

STAR Collaboration: J. Adams (2005). Experimental and Theoretical Challenges in the Search for the Quark Gluon Plasma: The STAR Collaboration's Critical Assessment of the Evidence from RHIC Collisions. *arXiv e-prints*, nucl-ex/0501009, nucl–ex/0501009.

Steinheimer, J., Motornenko, A., Sorensen, A., Nara, Y., Koch, V. and Bleicher, M. (2022). The high-density equation of state in heavy-ion collisions: constraints from proton flow. *Eur. Phys. J. C 82*(10), 911.

Steinheimer, J. and Randrup, J. (2012). Spinodal amplification of density fluctuations in fluid-dynamical simulations of relativistic nuclear collisions. *Phys. Rev. Lett. 109*, 212301.

Steinheimer, J., Randrup, J. and Koch, V. (2014). Non-equilibrium phase transition in relativistic nuclear collisions: Importance of the equation of state. *Phys. Rev. C 89*(3), 034901.

Stoecker, H. and Greiner, W. (1986). High-Energy Heavy Ion Collisions: Probing the Equation of State of Highly Excited Hadronic Matter. *Phys. Rept. 137*, 277–392.

Sun, K.-J., Chen, L.-W., Ko, C. M., Pu, J. and Xu, Z. (2018). Light nuclei production as a probe of the QCD phase diagram. *Physics Letters B 781*, 499–504.

Sun, K.-J., Chen, L.-W., Ko, C. M. and Xu, Z. (2017). Probing QCD critical fluctuations from light nuclei production in relativistic heavy-ion collisions. *Physics Letters B 774*, 103–107.

Sun, K.-J., Ko, C. M., Li, F., Xu, J. and Chen, L.-W. (2021). Enhanced yield ratio of light nuclei in heavy ion collisions with a first-order chiral phase transition. *European Physical Journal A 57*(11), 313, 313.

CURRICULUM VITAE

Name: Thiranat Bumnedpan

Date of Birth: 1 June 1999

Place of Birth: Nakhon Ratchasima, Thailand

Educations:

- 2018-2022: School of Physics, Science, Suranaree University of Technology, Nakhon Ratchasima, Thailand (Bachelor of Science)
- 2022-2025: School of Physics, Science, Suranaree University of Technology, Nakhon Ratchasima, Thailand (Master of Science)

Grants and Fellowship:

Development and Promotion of Science and Technology Talents Project (DPST)

Publications:

- Bumnedpan, T., Steinheimer, J., Bleicher, M., Limphirat, A., and Herold,C. (2022). Enhanced pion-to-proton ratio at the onset of the QCD phase transition. Physics Letters B 835, 137537.
- Bumnedpan, T., Steinheimer, J., Reichert, T., Herold, C., Limphirat, A., and Bleicher, M. (2025). Time evolution of light nuclei cumulants and ratios with a first-order phase transition in the UrQMD transport model. Phys. Rev. C 111, 034910.